A Climatology of Strong Large-Scale Ocean Evaporation Events. Part I: Identification, Global Distribution, and Associated Climate Conditions

Franziska Aemisegger

Centre for Environmental and Climate Research, Lund University, Lund, Sweden, and Institute for Atmospheric and Climate Science, ETH Zurich, Zurich, Switzerland

Lukas Papritz

Geophysical Institute, University of Bergen, and Bjerknes Centre for Climate Research, Bergen, Norway

ABSTRACT

This paper presents an object-based, global climatology (1979–2014) of strong large-scale ocean evaporation (SLOE) and its associated climatic properties. SLOE is diagnosed using an "atmospheric moisture uptake efficiency" criterion related to the ratio of surface evaporation and integrated water vapor content in the near-surface atmosphere. The chosen Eulerian identification procedure focuses on events that strongly contribute to the available near-surface atmospheric humidity. SLOE is particularly frequent along the warm ocean western boundary currents, downstream of large continental areas, and at the sea ice edge in polar regions with frequent cold-air outbreaks. Furthermore, wind-driven SLOE occurs in regions with topographically enforced winds. On a global annual average, SLOE occurs only 6% of the time but explains 22% of total ocean evaporation. An analysis of the past history and fate of air parcels involved in cold season SLOE in the North Atlantic and south Indian Oceans shows that cold-air advection is the main mechanism that induces these events. Extratropical cyclones thereby play an important role in setting the necessary equatorward synoptic flow. Consequently, the interannual variability of SLOE associated with the North Atlantic Oscillation and the southern annular mode reveals a very high sensitivity of SLOE with respect to the location of the storm tracks. This study highlights the strong link between transient synoptic events and the spatiotemporal variability in ocean evaporation patterns, which cannot be deduced from thermodynamic steady-state and climate mean state considerations alone.

1. Introduction

Large-scale ocean evaporation is a key mechanism linking the energy and water budgets of oceans and the atmosphere (Baumgartner and Reichel 1975; Schmitt 1995; Trenberth and Caron 2001). Because of its efficiency in transferring energy between these two climate components (Kiehl and Trenberth 1997), ocean evaporation plays a fundamental role for the diabatic forcing of the atmosphere in middle and subpolar latitudes as well as for ocean deep convection events via associated cooling of surface waters and salinity changes (Talley 2008). In addition, it is a major contributor to high-impact weather, for example, by favorably preconditioning the atmosphere for rapid cyclone intensification (e.g.,

Yau and Jean 1989; Reed et al. 1993; Uotila et al. 2011; Kuwano-Yoshida and Minobe 2017) and polar low development (e.g., Rasmussen and Turner 2003), as well as downstream of the evaporation region in the form of heavy precipitation associated with the subsequent coherent transport of the evaporate (e.g., Winschall et al. 2012). The adequate representation of the large-scale conditions leading to strong atmospheric moisture uptake in numerical weather prediction and climate models is thus key for the design and operation of effective early warning systems and reliable climate forecasts alike.

Studying atmospheric moisture uptake resulting from surface evaporation on synoptic spatiotemporal scales provides important information about the atmospheric branch of the water cycle and the weather systems driving moisture transport. Sources of moisture for the atmosphere have been investigated in the literature from two different perspectives [see Gimeno et al. (2012) for a

Corresponding author: Franziska Aemisegger, franziska.aemisegger@env.ethz.ch

recent review]: the Lagrangian perspective is based on 3D-kinematic trajectories (e.g., Massacand et al. 1998; Sodemann et al. 2008a) and the Eulerian perspective uses tracers implemented in numerical climate and weather prediction models (e.g., Joussaume et al. 1986; Koster et al. 1986; Sodemann et al. 2009). Both methods allow for the identification of the sources, the so-called footprint, of the moisture advected to a specific region of interest. In particular, they have provided important insights into moisture transport mechanisms, the climatological sources of precipitation (e.g., Johnsen et al. 1989; Sodemann and Stohl 2009), and have contributed toward a better understanding of the precursors of heavy precipitation events (e.g., Winschall et al. 2012; Grams et al. 2014).

In this paper, we aim to investigate mid- and high-latitude environments that lead to favorable conditions for strong moisture fluxes from the ocean surface into the atmosphere. In particular, we focus on transient events with a notable impact on the near-surface atmospheric moisture budget. We present a methodology for an object-based climatological analysis of such events. This methodology provides the basis for a general Eulerian moisture source characterization using reanalysis data and can be easily applied to large datasets such as long-term climate simulations to effectively identify hot spots of strong moisture uptake by the atmosphere. As shown by Aemisegger and Sjolte (2018, hereinafter Part II), the proposed identification scheme can be applied for an in-depth investigation of the influence of environmental conditions prevailing during ocean evaporation for the climate signals recorded in the stable water isotope composition of atmospheric moisture.

Events of intense moisture transfer from the ocean to the atmosphere have been shown in the past from field experiments and from reanalysis data to occur in the cold sector of winter storms. The cold sector is characterized by high surface wind speeds and dry air (Bond and Fleagle 1988; Blanton et al. 1989), part of which descended from upper levels during dry-air intrusions (Browning 1997; Raveh-Rubin 2017). During the Fronts and Atlantic Storm Track Experiment (FASTEX), a composite analysis from ship measurements revealed low 10-m specific humidities and large surface latent heat fluxes (SLHs) behind the cold front ($-200\,\mathrm{W\,m^{-2}}$, where negative values indicate ocean heat loss), whereas smaller composite fluxes of $-150\,\mathrm{W\,m^{-2}}$ were measured ahead of cold fronts in the moist warm sector of the cyclone (Persson et al. 2005). Particularly over the warm ocean western boundary currents (WBCs), where the climatological SLHs are also large, storm passages can be accompanied by very large SLHs that can reach $-1500\,\mathrm{W\,m^{-2}}$ (Giordani and Caniaux 2001;

Moore and Renfrew 2002; Gulev and Belyaev 2012; Grist et al. 2016; Vannière et al. 2017; Bentamy et al. 2017). Object-based composite analyses of extratropical cyclones and their associated air–sea fluxes in the North Atlantic and the Southern Ocean have shown that the ocean loses more heat outside of the cyclones than inside (Yuan et al. 2009; Rudeva and Gulev 2011; Papritz et al. 2014). In fact, these studies highlight large areas of strong ocean evaporation located far to the west of the cyclone's core. Especially over the WBCs and at high latitudes, the advection of cold and dry polar air off the continent or the sea ice edge over open ocean during so-called cold-air outbreaks (CAOs; Grossman and Betts 1990; Bracegirdle and Kolstad 2010) is a major contributor to wintertime mean ocean evaporation (Papritz et al. 2015; Papritz and Spengler 2017). As these cold CAOs constitute the aforementioned cold sector of extratropical cyclones, they are closely linked to the cyclonic circulation and their associated frontal systems that can extend out farther equatorward from the cyclone system. Therefore, variations in the frequency of extratropical cyclones and fronts are strongly imprinted on the frequency of CAOs and the wintertime mean SLH (Papritz et al. 2015). In the present study, the linkage of strong ocean evaporation to extratropical cyclones and CAOs will be explored further using an object-based approach.

On seasonal–interannual time scales, the anomalies found in air–sea variables associated with the leading modes of atmospheric variability in both hemispheres, the North Atlantic Oscillation (NAO) and the southern annular mode (SAM), are relevant for the interpretation of the moisture source climate signals recorded in stable water isotope data of ice cores (Appenzeller et al. 1998; Sodemann et al. 2008a; Sjolte et al. 2011). Variability in strong ocean evaporation will thus be discussed in this paper along with relevant changes in the air–sea climate conditions for the different phases of the NAO and the SAM.

This study is organized as follows. First, a simple Eulerian framework is presented that identifies large-scale coherent areas where ocean water evaporates into a dry near-surface atmosphere, referred to as strong large-scale ocean evaporation (SLOE). The occurrence frequencies, seasonalities, and conditions associated with such events are subsequently discussed. Second, the history and fate of air masses involved in SLOE are analyzed using a Lagrangian perspective for two selected locations with frequent occurrence of SLOE in the North Atlantic and in the south Indian Ocean. Finally, anomalies in the occurrence frequency of SLOE events associated with dominant regional patterns of atmospheric circulation variability are discussed.

2. Dataset and methodology

a. Datasets

The climatological analysis of strong ocean evaporation is based on 6-hourly global ERA-Interim data (Dee et al. 2011) from the European Centre for Medium-Range Weather Forecasts (ECMWF) during the period 1979–2014. The meteorological fields used from the ERA-Interim dataset are interpolated from a T255 spectral resolution to a regular horizontal grid of 1° resolution with 60 vertical levels.

The quality of the ERA-Interim dataset varies with geographic location and depends on the density of the available observations. Near-surface humidity and its variations are reasonably well represented (Simmons et al. 2010; Pfahl and Niedermann 2011). SLHs being derived from short-term forecasts rely on the quality of the parameterizations used and the accuracy of the representation of the atmospheric state. Even though differences in SLH fields between available reanalysis products exist (Trenberth et al. 2011), the ERA-Interim estimates have been shown to perform well in the mid-to-high latitudes of the Northern Hemisphere (NH) and outperform other reanalyses (Renfrew et al. 2002; Moore and Renfrew 2002; Renfrew et al. 2009; Lindsay et al. 2014). The observational constraint on the atmospheric state in the Southern Hemisphere (SH) is somewhat weaker than in the NH and the uncertainties associated with the air–sea reanalysis fields are expected to be higher. However, the disparity between the two hemispheres, at least in terms of the performance of the 500-hPa geopotential height forecasts averaged over the hemispheres has nearly disappeared, as shown by Dee et al. (2014); thus, we do not expect the uncertainties to be large. Furthermore, the physical consistency given by the reanalysis framework and its global spatiotemporal coverage are crucial for this study.

One important source of uncertainty in surface fluxes is related to the boundary conditions provided by the SST. Rouault et al. (2003) showed evidence for a considerable underestimation of the SLH in ECMWF and NCEP reanalyses along the Agulhas Current compared to estimates from in situ data collected during two ship cruises. The authors thus highlight the difficulty the models have in adequately representing the 80–100-km-wide core of the Agulhas Current and the sharp sea surface temperature (SST) gradients associated with it. Similar problems have to be expected over other narrow warm ocean surface currents, as well as in regions of strong SST gradients such as in the region of the Brazil Current (Pezzi et al. 2016). This is all the more relevant as the resolution of the prescribed SST in ERA-Interim increased substantially over the period considered here,

with a strong influence on surface evaporation along the Gulf Stream front (Parfitt et al. 2017). Such biases can, thus, become particularly important along the warm WBCs, and they may have a major impact on the atmospheric moisture budget resulting from large SLH found in these regions. Despite these biases, we would like to stress that reanalysis makes it possible to study climatological surface fluxes that were computed from instantaneous fields, which is considerably more accurate than using mean fields (cf. Simmonds and Dix 1989).

b. Definition and identification of strong large-scale ocean evaporation

1) ATMOSPHERIC MOISTURE UPTAKE EFFICIENCY CRITERION

The parameterization of net SLH (negative upward) for ERA-Interim [i.e., in the ECMWF Integrated Forecasting System (IFS) cycle 31] is based on the following relation (ECMWF 2007):

$$\mathrm{SLH} = \rho \lambda C_e |U|(q_a - q_s), \tag{1}$$

where ρ is the air density, λ is the latent heat of vaporization, C_e is the nondimensional transfer coefficient for moisture determined by the atmospheric stability following a Monin–Obukhov formulation, $|U|$ is the instantaneous wind speed at the first model level (at ~10 m), q_s is the saturation specific humidity with respect to SST, and q_a is the specific humidity at the first model level. For a detailed discussion of the impact of approximations and assumptions in the ECMWF parameterization of SLH and comparison with other parameterizations we refer to Brodeau et al. (2017).

The ocean evaporation rate E (positive upward) can then be determined from the SLH:

$$E = \frac{-\mathrm{SLH}}{\rho_w \lambda}, \tag{2}$$

with ρ_w being the density of liquid water. The humidity gradient between the ocean surface and the first model level (corresponding to ~10 m above the surface), $\Delta q = q_s - q_a$, can also be expressed in terms of a normalized relative humidity calculated with respect to the interface conditions (SST and surface pressure),

$$h_s^{10\mathrm{m}} = \frac{q_a}{q_s}. \tag{3}$$

This relative humidity at 10 m normalized to SST $h_s^{10\mathrm{m}}$ is a key quantity for the parameterization of isotope evaporation (Craig and Gordon 1965; Horita et al. 2008). It will be used subsequently as an important

climate characteristic for atmospheric moisture uptake resulting from strong ocean evaporation.

Most existing object-based studies that focus on events of strong air–sea freshwater fluxes (evaporation or precipitation) define such events in terms of the exceedance of a gridpoint-based threshold, defined by a local climatological percentile of the flux (e.g., Pfahl and Wernli 2012; Catto and Pfahl 2013; Papritz et al. 2015). In this study, we are interested in strong evaporation events, which lead to substantial moisture uptake by the atmosphere compared to the near-surface water vapor content already present before the uptake occurs. In this sense, these events become an important or even dominant moisture source (Sodemann et al. 2008a) for a given air mass. We thus based our identification of strong, large-scale ocean evaporation features on a criterion that relates the moisture flux into the atmosphere by ocean evaporation to the vertically integrated moisture content of the atmosphere in a 20-m-thick layer above the ocean surface. Specifically, we define SLOE objects as interconnected grid cells (each grid cell must touch another grid cell within one given object), where the atmospheric moisture uptake efficiency f_{evap}[1] exceeds a certain threshold. Thereby, f_{evap} is defined as

$$f_{evap} = \frac{E}{IWV^{20m}}, \quad (4)$$

where IWV^{20m} is the vertically integrated water vapor content in the lowest 20 m of the atmosphere; that is, $IWV^{20m} = q(p_0 - p_{\ell 1})/\rho_w g$ with q the specific humidity at the first model level, p_0 the surface pressure, $p_{\ell 1}$ the pressure at the interface between model levels 1 and 2, and $g = 9.81 \text{ m s}^{-2}$ the acceleration due to gravity. Note that the first model-layer thickness is on average about $\Delta p = \sim 2.4$ hPa (corresponding to ~ 20 m). In addition, for the discretized form of IWV used here, we assumed a constant vertical profile of q between p_0 and $p_{\ell 1}$. Linear interpolation between the saturated specific humidity at the surface and the specific humidity at the first model level could be performed as an alternative, which leads to systematically higher IWV^{20m} and lower f_{evap} but does not otherwise change the shape of the objects or the climatological analysis. The uptake efficiency f_{evap} can be interpreted as a simplified inverse residence time of moisture in the lowest model layer. It ensures that the identified evaporation events contribute strongly to the available near-surface atmospheric humidity, leading to a considerable and sustained modulation

of the stable water isotope composition of low-level atmospheric vapor (e.g., Gat et al. 2003; Kurita 2011; Aemisegger 2013).

The f_{evap} threshold value chosen here for delimiting SLOE features is 1.5 h^{-1}. This value corresponds approximately to the 80th percentile of the f_{evap} distribution and was chosen by visual inspection of 6-hourly ERA-Interim fields such as are shown in Fig. 1 and by testing different threshold values. Given the chosen threshold and the 6-hourly temporal resolution of the ERA-Interim data, the integrated moisture input into the atmosphere by surface evaporation has to be at least 9 times larger than IWV^{20m}. As will be discussed in section 3b, using this f_{evap} threshold leads to a global average occurrence frequency of 6% explaining 22% of the total annual ocean evaporation. The average geographical extent and number of identified areas of strong ocean evaporation are sensitive to the choice of this threshold value. Values between 0.5 and 2.5 h^{-1} have been tested and lead to qualitatively similar results. Naturally, the explained part of the ocean evaporation and occurrence frequencies of SLOE is higher (lower) when using threshold values below (above) $f_{evap} = 1.5 \text{ h}^{-1}$. The results of the sensitivity study are discussed later in section 3b.

Since we are interested in large-scale evaporation events that play an important role as an atmospheric moisture source and are triggered by extratropical synoptic-scale weather systems, we only consider features with a certain minimum geographic extent (outermost contour ≥ 2000 km). This criterion is implemented by selecting only SLOE objects from the f_{evap} field that have a f_{evap} threshold (here $f_{evap} = 1.5 \text{ h}^{-1}$) contour length of at least 2000 km. Binary 6-hourly SLOE masks are thus defined by assigning a flag value of 1 to grid cells fulfilling the above criteria and a 0 otherwise. Grid points over land or sea ice are not considered in the analysis. The SLOE occurrence frequency over a given period is then computed as the temporal average of the binary 6-hourly SLOE masks. A SLOE frequency of 50% thus implies that in half of the 6-hourly fields a given grid cell is located within a SLOE feature. Composites of a particular field F during SLOE are computed as temporal averages (in angle brackets) only considering time steps with SLOE, denoted as $\langle F|_{SLOE}\rangle$. Similarly composites in the absence of SLOE (no SLOE) are computed and denoted as $\langle F|_{noSLOE}\rangle$.

In contrast to an approach that would identify strong evaporation objects with a fixed SLH threshold, the diagnostic presented here overcomes a strong latitudinal sensitivity of the identification procedure by relating the moisture flux into the atmosphere to the amount of humidity that is already present. This allows us to focus

---

[1] Note, that we use the term atmospheric moisture uptake efficiency for f_{evap} in analogy to the concept of precipitation efficiency relating precipitation to its sources of formation (Braham 1952).
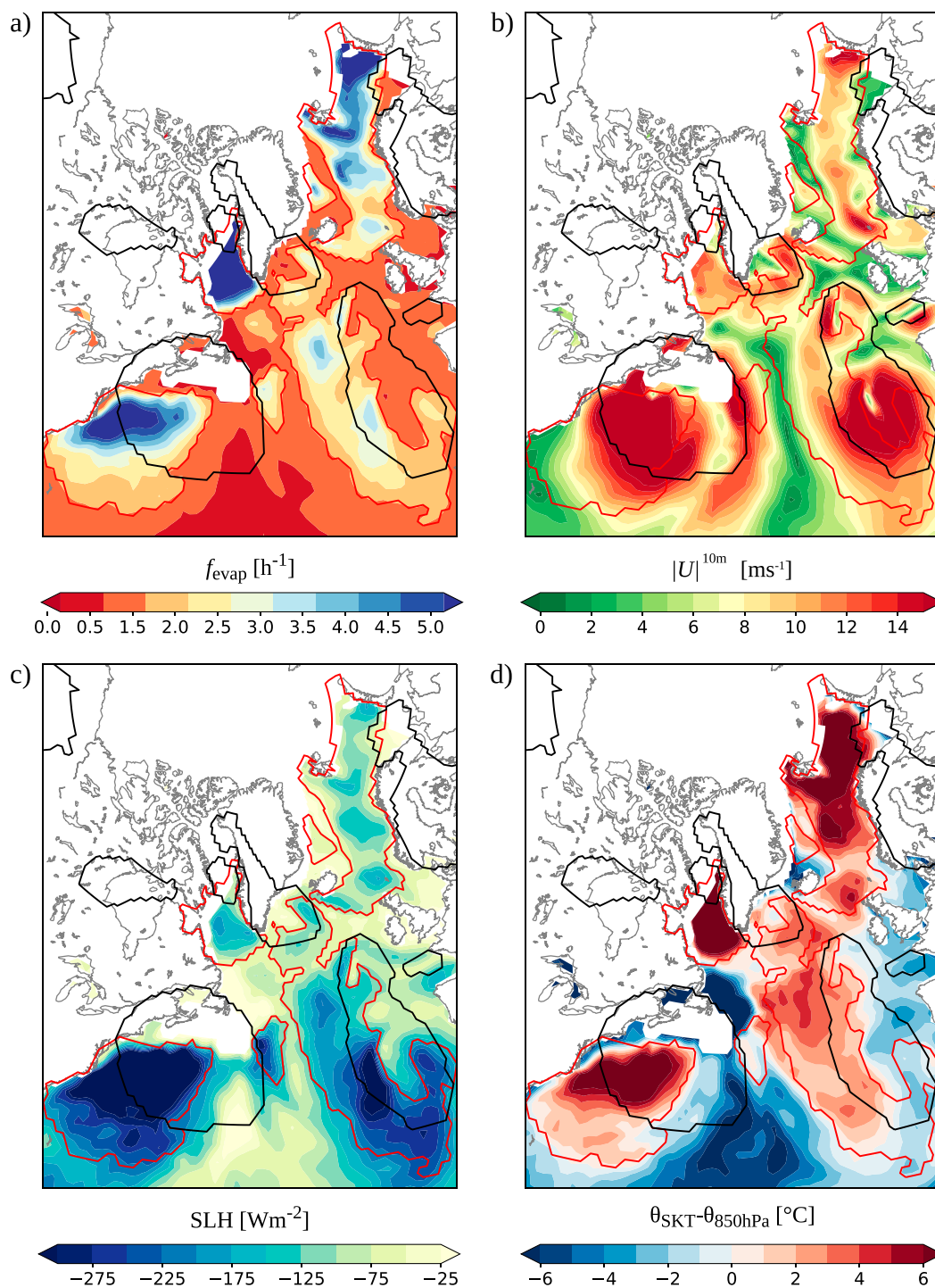
FIG. 1. Identification example of SLOE over the North Atlantic using the evaporation efficiency parameter $f_{\text{evap}} \geq 1.5\,\text{h}^{-1}$ at 1800 UTC 1 Mar 2010. All panels show identified SLOE objects (red contours) and the cyclone regions (black contours). The shading shows (a) f_{evap}, (b) $|U|^{10m}$, (c) SLH, and (d) $\theta_{\text{SKT}} - \theta_{850\,\text{hPa}}$. Areas with SLH $> 0\,\text{W}\,\text{m}^{-2}$ or sea ice concentration $>50\%$ as well as land areas are masked.

on the contribution of evaporation to the near-surface humidity budget rather than the absolute flux, which strongly depends on temperature and thus on the latitude. Our methodology is intentionally kept simple and computationally cheap such that it can easily be applied to large datasets from long-term climate simulations. The SLOE approach could, thus, for example, be used to investigate changes in moisture source conditions over climatic time scales. Furthermore, the presented identification procedure of SLOE events can be thought of as a complementary Eulerian counterpart to the Lagrangian moisture source identification method (Sodemann et al. 2008a), which is widely used in isotope studies to diagnose conditions at the evaporative moisture source.

2) ASSOCIATION WITH EXTRATROPICAL CYCLONES

Extratropical cyclones are identified using a slightly updated version (Sprenger et al. 2017) of the algorithm of Wernli and Schwierz (2006). Regions within closed sea level pressure (SLP) contours that contain one or several local sea level pressure minima are defined as cyclone masks. The maximum length of the outermost pressure contour is restricted to 7500 km. The cyclone occurrence frequency over a given period is computed, similarly to the description of the SLOE occurrence frequency, as the temporal average of binary cyclone mask fields, in which cyclone regions are flagged with 1 and noncyclone regions with 0. The association of a SLOE feature with a cyclone is based on a simple collocation criterion with the restriction that at least 1% of the area of a coherent SLOE object has to overlap with a cyclone object. Note that the association of SLOE with cyclones becomes stronger for lower f_{evap} thresholds because of larger SLOE features and weaker for higher f_{evap} thresholds. While globally 88% of the SLOE events are associated with cyclones for an f_{evap} threshold of $0.5\,h^{-1}$, the association percentage drops to 59% (49%) for an f_{evap} threshold of $1.5\,h^{-1}$ ($2.5\,h^{-1}$). The SLOE identification example discussed in the next section illustrates the expected strong connection of SLOE with extratropical cyclones. It has to be noted that the area affected by the cyclone-induced circulation can be larger than the region encompassed by the outermost closed SLP contour. In such cases, the association of a SLOE event with a cyclone is missed with this method. We thus expect the SLOE–cyclone association numbers obtained here to be a lower bound.

3) IDENTIFICATION EXAMPLE

To provide a concrete picture of SLOE events at the synoptic time scale, Fig. 1 shows an example of different relevant air–sea variables over the North Atlantic,

including masks of SLOE objects and delineated cyclone areas at 1800 UTC 1 March 2010. As expected from Eq. (1), large SLH, which is characteristic of SLOE (Fig. 1c), predominantly occur in areas with low h_s^{10m} or strong 10-m wind speeds $|U|^{10m}$ (Fig. 1b). These regions coincide further with large positive potential temperature differences between the sea surface and the air at 850 hPa ($\theta_{SKT} - \theta_{850hPa}$; Fig. 1d), indicative of cold-air advection. In this example, the SLOE features with the largest f_{evap} are located in the Labrador Sea, along the U.S. East Coast, and the Nordic seas and Barents Sea (Fig. 1a). They are associated with the cold sector of extratropical cyclones.

c. Air-parcel trajectory calculations

For the cold season (boreal DJF, austral JJA) kinematic backward and forward air-parcel trajectories are calculated based on the three-dimensional winds using version 2.0 of the Lagrangian analysis tool (LAGRANTO) (Wernli and Davies 1997; Sprenger and Wernli 2015). The trajectories are started from two points. The first point is chosen in the North Atlantic near the Gulf Stream frontal zone (40°N, 60°W; cf. Fig. 2) and the second in the south Indian Ocean between the subtropical and Agulhas fronts (43°S, 59°E). From each point trajectories are started from the lowest model level corresponding to a starting altitude of approximately 10 m above the ocean surface and calculated 5 days forward as well as backward in time. The trajectory position is written out in six hourly intervals and complementary meteorological variables are interpolated to the position of the trajectory, thus providing different characteristics of the air parcels. The data are separated into two groups for the analysis: one containing all trajectories that are associated with SLOE at the starting point and another with the trajectories that do not fulfill this criterion. To provide an overview of the air parcels' origin and fate when involved in SLOE compared to the reference case without SLOE, the trajectory positions are gridded 72 h before arrival and after departure from the selected starting point. Depending on the starting point, approximately 45%–65% of the trajectories are associated with a strong, large-scale ocean evaporation event.

3. Climatological properties

a. Global distribution

The global distribution of the annual SLOE occurrence frequency (Fig. 2a) emphasizes three categories of SLOE: 1) warm-ocean evaporation along the WBCs, 2) wind-driven evaporation southwest of the cyclone
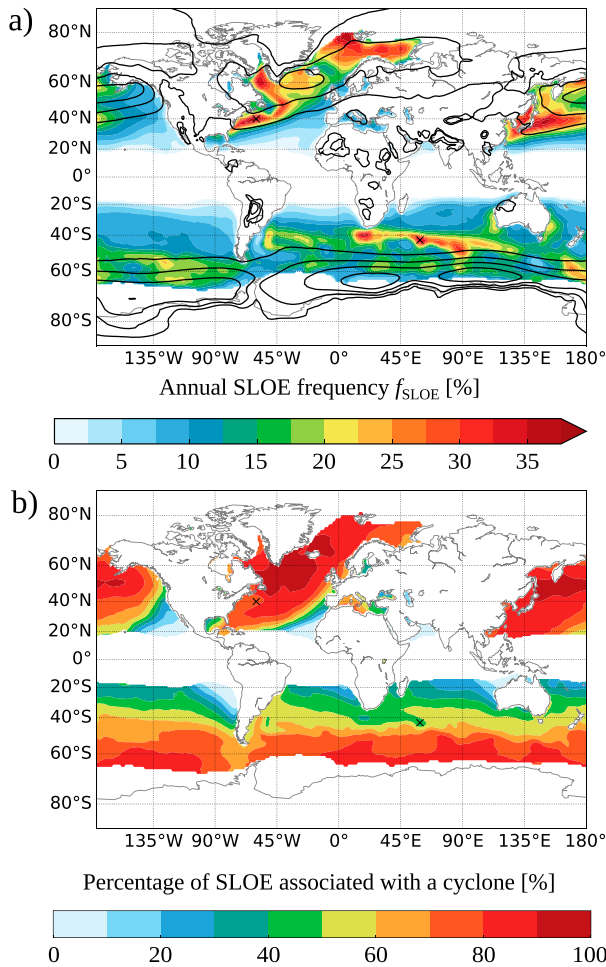
FIG. 2. (a) Global distribution of annual occurrence frequency of SLOE (1979–2014; shaded) with cyclone frequency between 10% and 40% in steps of 10% in black contours and (b) percentage of SLOE associated with a cyclone. The crosses in the North Atlantic and the south Indian Oceans indicate the starting points of the Lagrangian analysis presented in section 3d. Land areas and areas with seasonal sea ice are masked.

frequency maximum in the Irminger Sea and northward of the cyclone frequency maxima in the south Indian Ocean, and 3) polar-air evaporation during CAOs at high latitudes. This categorization emerges from the synthesis of the analysis of different aspects of SLOE properties, as will be illustrated in the following results sections. The chosen terminology highlights one of the three most important prerequisites for each category, namely warm ocean, strong winds, and cold air based on the distinct climate conditions associated with each SLOE type (see section 3c). For reference Fig. 3 shows the annual mean SST along with the ocean currents and geographic names used in the following.

There is a strong seasonality to the SLOE frequencies in the NH with changes in the range of 20%–50%

between summer and winter. In particular, along the Gulf Stream, SLOE frequencies of 50%–70% are observed during the winter, whereas SLOE frequencies drop to 1%–5% in summer, when weaker land–sea temperature contrasts and strong continental evaporation leads to the advection of warmer and more humid air masses over the ocean basins (Fig. 4a and Fig. B1 in appendix B). The surface humidity gradients are thus much weaker in the warm season and so are surface wind speeds due to the reduced storminess. The seasonal cycle in the SH is not as pronounced as in the NH, with SLOE frequencies of 10%–20% even in summer along the Agulhas Return Current.

Hot spots of warm-ocean evaporation are found in the NH along the Gulf Stream in the North Atlantic and the Kuroshio in the Pacific, with annual-mean occurrence frequencies that are in excess of 35%. In the SH the Agulhas Retroflection, the Agulhas Return Current, as well as its prolongation into the south Indian Ocean stand out with a band of several zonally aligned maxima of SLOE frequencies of approximately 30%. The midlatitude belts of high atmospheric moisture uptake efficiency f_{evap} (Fig. 5b) and SLOE frequency (Fig. 2a) in the south Indian Ocean follow the warm SST (Fig. 3) along a spiralform path toward Antarctica. Slightly lower SLOE frequencies of approximately 20% are found along the Brazil Current, and along the west and east coasts of Australia. The regional maxima in occurrence frequencies of SLOE along the WBCs are collocated with prominent extratropical maxima in ocean evaporation (Fig. 5a).

The wind-driven SLOE events in the NH occur in the regions with the overall highest wind speeds found over the NH oceans: the Irminger Sea and south of Bering Strait (Sampe and Xie 2007). High wind speeds in these regions are related to the interaction of extratropical cyclones with steep orography causing intense tip jets and barrier winds, and they are often concomitant with a CAO, thus, favoring intense evaporation (e.g., Doyle and Shapiro 1999; Våge et al. 2009; Harden et al. 2011; Moore and Pickart 2012; Papritz 2017). In particular, tip jets off the southern tip of Greenland are known to strongly enhance SLH and thereby contribute to dense water formation (Våge et al. 2009). Wind-driven SLOE in the Southern Ocean is found close to the sea ice edge in the south Indian Ocean, slightly to the north of the two cyclone frequency maxima.

Despite the relatively cold ocean surface waters in the Labrador and Irminger Seas, Nordic seas, and the Barents Sea, as well as along the Antarctic sea ice edge, locally high SLOE frequencies are found in these regions (Figs. 4a,c). These polar-air SLOE events occur exclusively during the cold season. The local maxima in
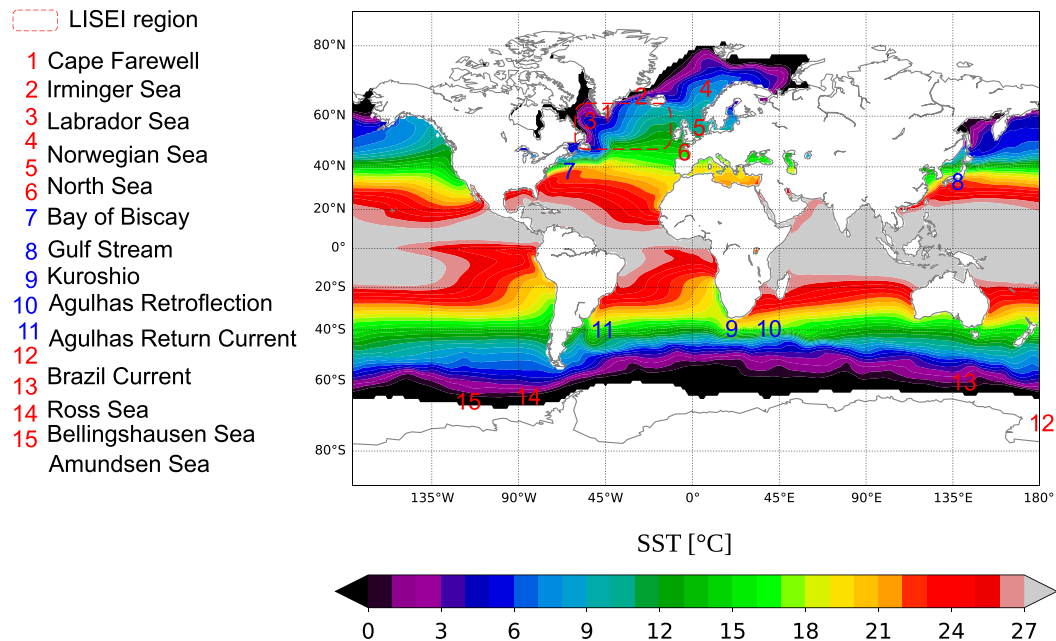
FIG. 3. Annual mean SSTs from the ERA-Interim dataset for the period 1979–2014. The names of the major ocean currents and seas used in the text are referenced in this figure. Regions with seasonal sea ice are masked. The red-dashed LISEI region is discussed in section 4a.

SLOE frequency are related to the preferred occurrence of marine CAOs, where radiatively cooled air masses with a large humidity deficit compared to the open-ocean surface saturation specific humidity are advected across the sea ice edge over the open ocean. These local maxima of SLOE occurrence frequency in the Ross, Amundsen, and Bellingshausen Seas (Papritz et al. 2015) in the SH, as well as in the Labrador and Irminger Seas, the Nordic seas, and the Barents Sea (Kolstad et al. 2009; Bracegirdle and Kolstad 2010; Papritz and Spengler 2017) in the NH, correspond to regions known for frequent CAOs.

The hot spots of warm-ocean SLOE along the WBCs are regions characterized by strong ocean–atmosphere coupling with high air–sea feedback strengths (Hausmann et al. 2017) and coincide with areas of large atmospheric heat transport divergence (e.g., Trenberth et al. 2001; Mayer and Haimberger 2012). Thus, warm-ocean SLOE mainly occurs in regions that are important for the rapid export of moisture. The mid-to-high-latitude regions with predominantly polar-air and wind-driven SLOE coincide with areas of convergence of heat and moisture in the annual mean (e.g., Trenberth et al. 2001; Mayer and Haimberger 2012).

Wintertime polar-air and wind-driven SLOE events in the NH are more persistent with average event durations of approximately 3 days compared to approximately 2.5 days for warm-ocean SLOE events along the WBCs (Fig. 4b). For example, in the North Atlantic this is due to the stationarity of cyclones developing in the lee of Greenland and slower propagation of cyclones at the end of the storm track than over the Gulf Stream, where cyclones are more transient. In contrast to the NH, polar-air SLOE events during the SH cold season are more short lived (~1.5 days) than in the NH and than SH warm-ocean SLOE events (~1.7 days).

The case study presented in section 2 suggests that cold-air advection and descending, dry air masses behind the cold front and within the cold sector of extratropical cyclones provide favorable conditions for SLOE. Indeed, more than 70% of SLOE events in the NH, as well as in the SH poleward of 50°S are directly associated with cyclones (Fig. 2b). In contrast to the NH, the SH fraction of SLOE associated with cyclones declines to 40% in the subtropics. The Southern Ocean and in particular the south Indian Ocean are known for the frequent occurrence of elongated, mobile cold fronts that extend from the SH storm track region equatorward as far as the subtropics (Simmonds et al. 2012; Schemm et al. 2015). These cold fronts separate relatively cold air masses from warmer subtropical air and thus likely play an important role in inducing SLOE events, in particular over the Agulhas Return Current. Additional mechanisms that can lead to SLOE in the subtropics include strong meridional flow induced by anticyclones, interaction with the jet (Cau et al. 2007), as well as dry air intrusions (Raveh-Rubin 2017).

a) Winter SLOE Frequency (NH: DJF, SH: JJA)

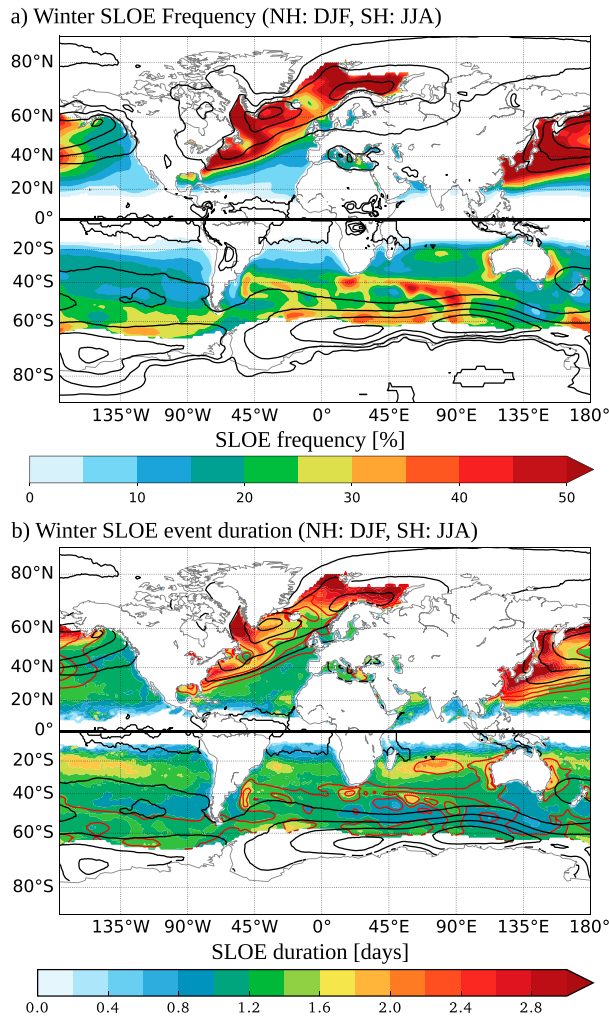

b) Winter SLOE event duration (NH: DJF, SH: JJA)

FIG. 4. Winter (DJF in NH and JJA in SH) SLOE (a) occurrence frequencies and (b) duration. The occurrence frequency of cyclones is shown from 10% to 40% in intervals of 10% (black contours). Land areas, regions with SLOE frequencies below 1%, or with seasonal sea ice are masked. The red contours in (b) show the SLOE frequency contours of 20%, 30%, and 40%.

FIG. 5. Annual mean (a) E and (b) f_{evap}. Land areas and areas with seasonal sea ice are masked.

Other notable, but slightly weaker local maxima in the occurrence frequencies of SLOE with values of up to 30% that do not clearly fit in the above three categories include the wintertime maximum in the Mediterranean region, particularly pronounced in the eastern part of the basin, as well as at around 30°S in the south Indian subtropical high pressure area. In other subtropical areas of both hemispheres, SLOE is relatively rare during all seasons with frequencies between 1% and 10%. These low SLOE occurrence frequencies close to the equator are explained by the climatologically high atmospheric moisture content in these regions, and, in the eastern oceanic basins also by the limitation of the SLHs as a result of the relatively colder SSTs.
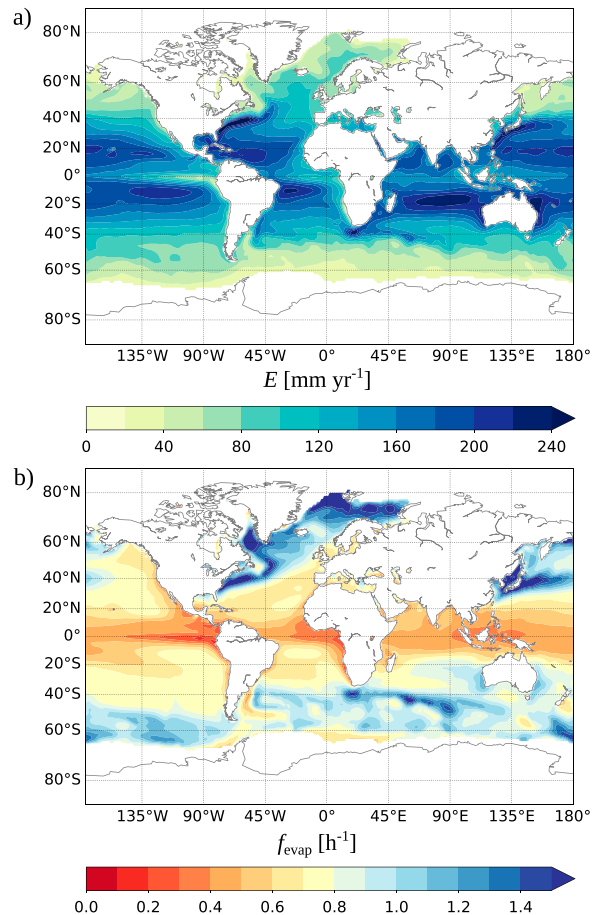
Consequently, the occurrence of SLOE in these regions requires incursions of drier air masses from the free troposphere and/or the extratropics. Such transport of drier air masses could, for instance, be affected by extratropical cyclones and their associated dry intrusions or be induced by the ageostrophic circulation associated with the subtropical jet. In the SH, the whole subtropical anticyclone belt is characterized by relatively persistent SLOE events with an average wintertime duration of 1.6–2 days.

b. Relevance of strong ocean evaporation events as a major moisture source for the atmosphere

With the atmospheric moisture uptake efficiency threshold defined here for SLOE events ($f_{evap} = 1.5\,h^{-1}$), 22% of total annual ocean evaporation is explained by SLOE and the annual-mean global occurrence frequency is 6%. If the threshold is set to $f_{evap} = 0.5\,h^{-1}$, then the global mean occurrence frequency rises to 33% and the explained fraction of evaporation to
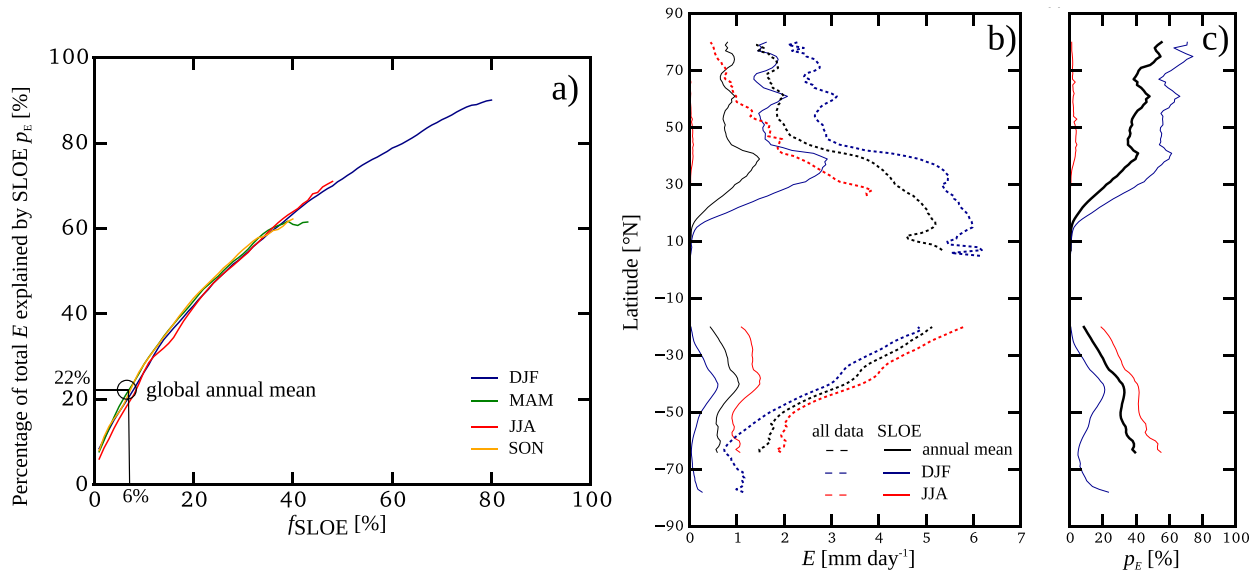
FIG. 6. (a) Percentage of total SLH explained by SLOE events as a function of the frequency of occurrence of these events. Moving window bins of 5% for the frequency of occurrence have been used for the computation of the average percentages of total SLH. The annual-mean SLOE occurrence frequency is 6% ± 9% with an explained fraction of total evaporation of 22% ± 17%. (b) Zonal mean of total evaporation (dashed) and SLOE evaporation (solid) for DJF and JJA. (c) Zonal mean of the percentage of explained evaporation by SLOE.

approximately 64%, and, in particular, tropical evaporation also gets partly classified as SLOE. If, on the other hand, the atmospheric moisture uptake efficiency parameter is increased to $f_{evap} = 2.5\,h^{-1}$, smaller-scale structures are obtained, the global annual occurrence frequency is lowered to 2%, and the evaporation explained by SLOE is reduced to approximately 11%. In this case, several SLOE objects per cyclone appear. Hence, it is mainly the size of the SLOE objects that differ among the tested thresholds. With the chosen f_{evap} threshold the composite winter SLOE SLH corresponds to the 25th percentile (note that SLH is defined negative upward) of the 6-hourly SLH distribution for the same season in the subpolar regions. In the subtropics, the SLOE composite SLH corresponds to the 5th–10th SLH percentiles.

The fraction of evaporation associated with SLOE events exceeds the frequency of occurrence of SLOE in all seasons (Fig. 6a). During winter the explained fraction of ocean evaporation is between 32% (SH) and 35% (NH) for SLOE occurrence frequencies of about 10%. In regions such as along the WBCs or at the sea ice edge, where SLOE events occur 40% of the time, they explain approximately 60% of the regional ocean evaporation. The ocean evaporation induced by SLOE (E_{SLOE}) shows a maximum in the zonal mean for both hemispheres at around 40° latitude (Fig. 6b) in winter, where SLOE explains approximately 40% for the SH and approximately 60% for the NH of the zonal-mean

ocean evaporation (Fig. 6c). In both hemispheres the percentage of zonal-mean ocean evaporation explained by SLOE is maximum at the poles and decreases toward the equator. The weaker seasonal cycle in the SH compared to the NH in total E, as well as in E_{SLOE}, is clearly visible in Fig. 6b.

It is noteworthy that the wintertime latitudinal maximum of E_{SLOE} in the NH is about twice as large as that in the SH. This emphasizes the significant contribution of warm-ocean SLOE over the Gulf Stream and the Kuroshio for the transfer of moisture and heat from the ocean to the atmosphere. Consequently, warm-ocean SLOE plays an important role as a diabatic source for the atmosphere, which could help explaining hemispheric differences and the relative contributions of atmosphere and ocean in the poleward heat transport (cf. Fasullo and Trenberth 2008).

c. Associated climate conditions

The Eulerian hot spots of strong atmospheric moisture uptake identified in section 3a coincide with climatological hot spots of Lagrangian moisture sources for precipitation at the continental scale such as Greenland in the North Atlantic (Sodemann et al. 2008a) and Antarctica in the Southern Ocean (Sodemann and Stohl 2009). Concomitant with the large fraction of evaporation explained by SLOE, this suggests that the conditions during SLOE events (Fig. 7) might play an important role in shaping the stable water isotope
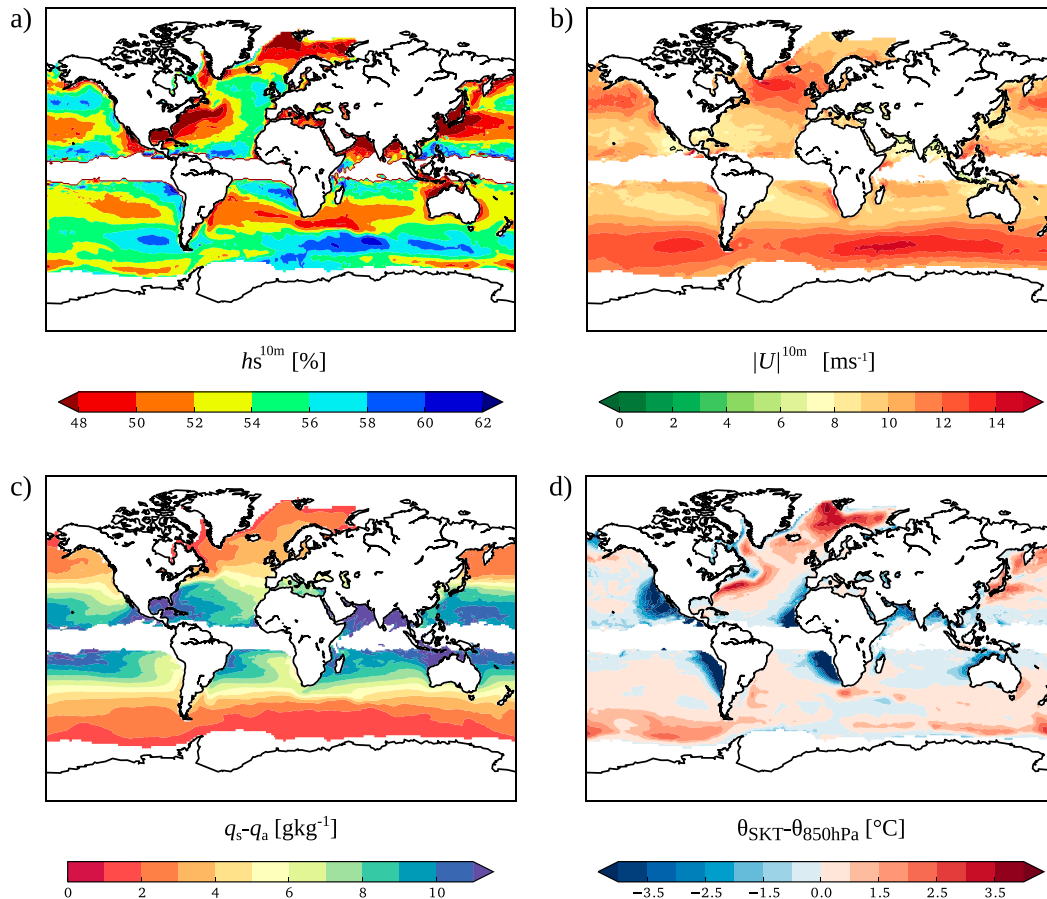
FIG. 7. Annual mean composite of (a) h_s^{10m}, (b) $|U|^{10m}$, (c) Δq, and (d) $\theta_{SKT} - \theta_{850hPa}$ during SLOE for the period 1979–2014. Data points where the frequency of occurrence of SLOE is below 1%, land areas, or regions with seasonal sea ice are masked.

signature of mid-to-high-latitude precipitation (Noone and Simmonds 2002).

The warm-ocean, wind-driven, and polar-air SLOE regimes are characterized by different typical humidity gradients between the ocean surface and 10 m above ($\Delta q = q_s - q_a$; Fig. 7c). While warm-ocean SLOE is associated with $\Delta q > 6$ g kg^{-1}, polar-air SLOE occurs at $\Delta q < 3$ g kg^{-1}. These two evaporation regimes are characterized by similar $h_s^{10m} = \sim 45\%$–50% (Fig. 7a). Higher h_s^{10m} in the range of approximately 55%–60% and $\Delta q = 2$–4 g kg^{-1} are associated with wind-driven SLOE with typical $|U|^{10m}$ of 12–14 m s^{-1}, which is clearly larger than $|U|^{10m} < 12$ m s^{-1} for the two other types (Fig. 7b).

The air–sea potential temperature difference, $\Delta \theta = \theta_{SKT} - \theta_{850hPa}$, is a measure of the stability of the lower troposphere with positive values characteristic of CAOs (e.g., Papritz et al. 2015; Papritz and Spengler 2017). Positive values during SLOE are thus found at high latitudes in the regions prone to intense CAOs (Fig. 7d).

In addition, warm-ocean SLOE over the Gulf Stream and the Kuroshio is also associated with positive albeit slightly weaker $\Delta \theta$. SLOE in the eastern subtropical ocean basins is associated with negative $\Delta \theta$. Specifically, in the subtropical northeastern Pacific and Atlantic the rarely occurring SLOE events are characterized by a strong humidity depletion of the air masses that are advected from very arid continental regions over the ocean (Figs. 7a,c). In the SH subtropical eastern Pacific and Atlantic the humidity gradients are much weaker, but $|U|^{10m}$ are higher than in their NH ocean basin counterparts.

To exemplify the differences between SLOE and no-SLOE conditions, we tabulate average conditions during SLOE in the North Atlantic (30°–90°N, 100°W–100°E) in Table 1 for the years 2010–14. Table 1 shows that the climate properties during SLOE clearly differ from average conditions. Typical SLOE h_s^{10m} is in the range 40%–60% whereas average conditions are generally associated with values in the range of 70%–90%

TABLE 1. Mean conditions during SLOE in the North Atlantic (30°–90°N, 100°W–100°E) during the period 2010–14.

	Mean	Std dev	10th percentile	90th percentile
h_s^{10m} (%)	53	8.8	41.2	63.6
SST (°C)	13.1	7.6	2.5	23.9
SLH (W m^{-2})	−178	81	−291	−74
BLH (m MSL)	1238	302	894	1575
$|U|^{10m}$ (m s^{-1})	9.1	3.2	4.7	13.4
q^{10m} (g kg^{-1})	5.5	2.8	2.3	9.1

(not shown). Also, larger than normal SLOE boundary layer heights between 900 and 1600 m are found, along with strong SLHs in the range from −74 to −300 W m^{-1}, dry 10-m air between 2 and 9 g kg^{-1}, and $|U|^{10m}$ in the range 5–13 m s^{-1}.

Over the entire ERA-Interim period, conditions F during SLOE compared to no SLOE ($\Delta F_{\text{SLOE}-\text{noSLOE}}$) in winter are summarized in Fig. 8 and confirm the specific analysis made above for SLOE objects in the North Atlantic during the period 2010–14. Only the differences in SLOE winter conditions are discussed here, because the SLOE frequencies are largest during this season, thus yielding the most robust estimates, but the results are similar for the other seasons. SLOE events are characterized by typically colder (1°–4°C for 10-m temperature T^{10m}; Fig. 8c), drier (1–3 g kg^{-1} for 10-m specific humidity q^{10m}; Fig. 8d), and windier near-surface air masses (2–3 m s^{-1} for $|U|^{10m}$, except over the NH WBCs; Fig. 8b) with changes of up to 200 W m^{-2} in surface evaporation. This is consistent with expected changes associated with cold-air advection compared to warm-air advection or zonal flow. The kinematically induced change in h_s^{10m} reaching between −30% and −20% (Fig. 8a) because of cold-air advection in the SLOE hotspot regions is one order of magnitude larger than what we would expect from thermodynamical steady-state changes (which typically amount to a few percent in h_s^{10m} for 2°–4°C change in temperature; Schneider et al. 2010).

d. History and fate of SLOE air masses in the North Atlantic and the south Indian Ocean

When looking at the Lagrangian evolution of different thermodynamic characteristics of SLOE air masses in the North Atlantic and the south Indian Ocean (Fig. 9), it becomes clear that these air masses undergo a stronger transformation of their properties than do no-SLOE air masses. SLOE air masses originate from farther poleward and deeper into the North American continent in the case of the North Atlantic than no-SLOE air masses (Figs. 9i,j; a more detailed analysis is in appendix A; see Fig. A1a).

Air parcels involved in wintertime SLOE over the North Atlantic take up 70% of their moisture content in the period from $t_a − 24$ h to $t_a + 12$ h after their arrival at time t_a at 40°N, 60°W (p_{NA}; red curve in Fig. 9a). More than 50% of the SLOE trajectories at p_{NA} continuously experience SLOE during this 36-h period (not shown). Potential temperature and specific humidity of the air masses leading to SLOE in the North Atlantic differ from no-SLOE air masses up to 120 h before their arrival, and they tend to stay more humid in the 120 h after their passage at p_{NA} (Figs. 9a,c). These SLOE trajectories are generally associated with a stronger descent for up to 72 h before their arrival at time t_a (Fig. 9e), after which they tend to stay at lower levels than no-SLOE trajectories. Air masses that are not involved in SLOE at p_{NA} tend to rain out in the time interval between $t_a − 12$ h and $t_a + 48$ h. Precipitation (Rtot) along p_{NA} SLOE trajectories is much lower than along no-SLOE trajectories until $t_a + 36$ h, but exceeds that of no-SLOE trajectories afterward (Fig. 9g). The water vapor taken up by SLOE air parcels might thus contribute to the latent heat release associated with the warm conveyor belt of a subsequent cyclone.

The trajectory-based analysis of wintertime history and the fate of air masses leading to SLOE in the south Indian Ocean at 43°S, 59°E (p_{SIO}) yields similar results as in the North Atlantic with the difference that the effect of land is nearly negligible. Hence, the differences in the thermodynamic quantities are less pronounced, which is consistent with the previously obtained Eulerian findings (Fig. 8). The uptake of humidity during SLOE at p_{SIO} is on average around 40% during the period from 24 h before to 24 h after their arrival at point p_{SIO}. At $t_a − 72$ h, the SLOE trajectories are located on average between 10° and 15° longitude westward as well as 5° and 10° latitude southward compared to the no-SLOE trajectories (Fig. 9j; see also Fig. A1c).

4. Interannual variability in the North Atlantic and the Southern Ocean

The close link between SLOE and cold-air advection by the flow associated with extratropical cyclones
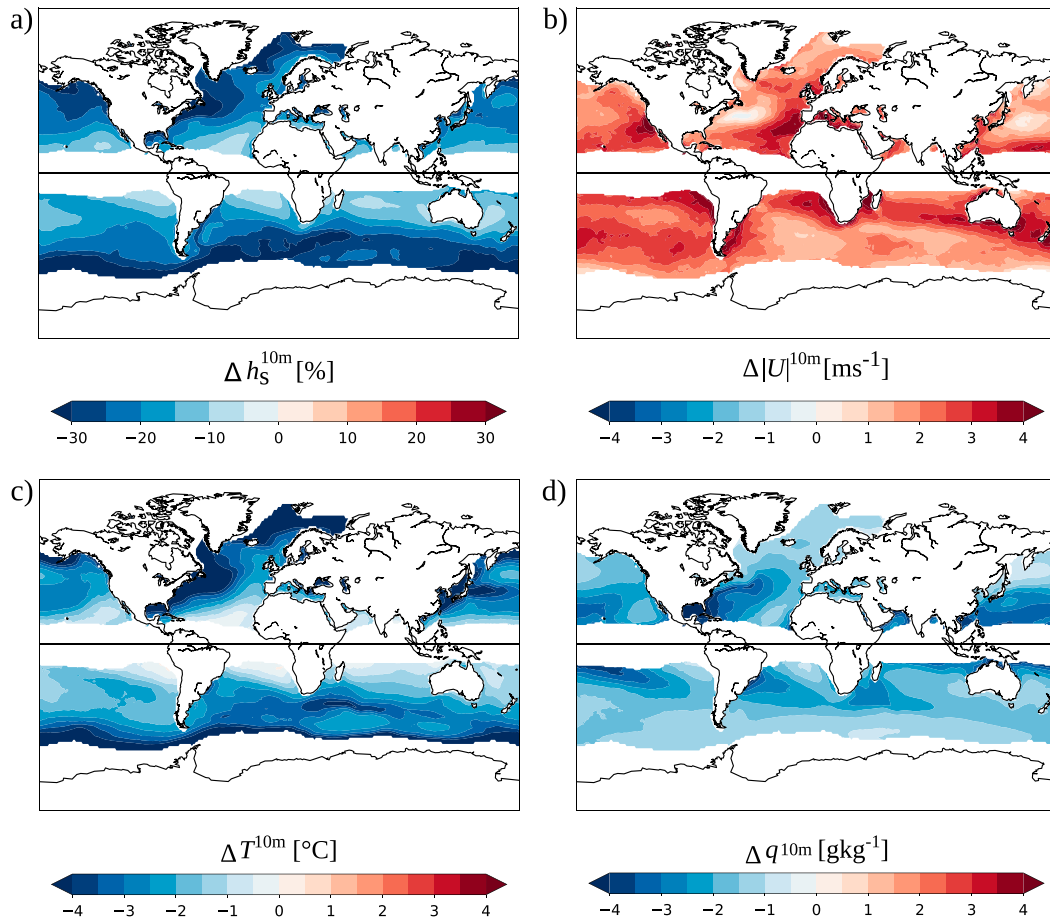
FIG. 8. Winter difference between conditions during SLOE and during no SLOE [$\Delta F_{\text{SLOE}-\text{noSLOE}} = \langle F|_{\text{SLOE}}\rangle - \langle F|_{\text{noSLOE}}\rangle$, with F representing the respective climate fields from (a)–(d) for DJF in NH and JJA in SH] over the period 1979–2014. The climate conditions are (a) h_s^{10m}, (b) $|U|^{10m}$, (c) T^{10m}, and (d) q^{10m}. The land areas, regions with SLOE frequencies below 1%, or with seasonal sea ice are masked.

(section 3b), indicates that the regional distribution of SLOE is strongly dependent on the position of the storm tracks. A poleward shift of the storm tracks is expected as a result of recent anthropogenic climate change (Shaw et al. 2016), which has an important impact on the frontal activity (Rudeva and Simmonds 2015) and the patterns of strong ocean evaporation. In the following, we discuss the causes of SLOE anomalies associated with two important variability patterns of the atmospheric circulation characterizing the strength and position of the storm tracks in the North Atlantic and the Southern Ocean. For that purpose, monthly station-based data of the NAO index (Walker and Bliss 1928; Hurrell 1995) and the SAM index (Marshall 2003) are used together with monthly mean fields of different SLOE variables to compute index-weighted seasonal composite differences between the positive and negative phases of the modes of variability. The anomaly patterns in air–sea variables are similar for

all seasons but strongest in winter. We thus focus on the winter season in the discussion below. The figures corresponding to summer are provided in appendix C.

a. SLOE variability associated with the North Atlantic Oscillation

The North Atlantic Oscillation (Hurrell 1995) has been related to the stable water isotope signature of precipitation and the accumulation records at different ice core drill sites in Greenland (White et al. 1997; Appenzeller et al. 1998; Vinther et al. 2003; Sjolte et al. 2011). During the negative phase of the NAO (NAO−), the moisture sources of precipitation have been found to be located in the southeastern North Atlantic (Sodemann et al. 2008a), consistent with the advection of moisture from more southerly locations caused by the stronger west–east elongation and southward shift of the storm track compared to the positive phase of the NAO (NAO+; Fig. 10, where
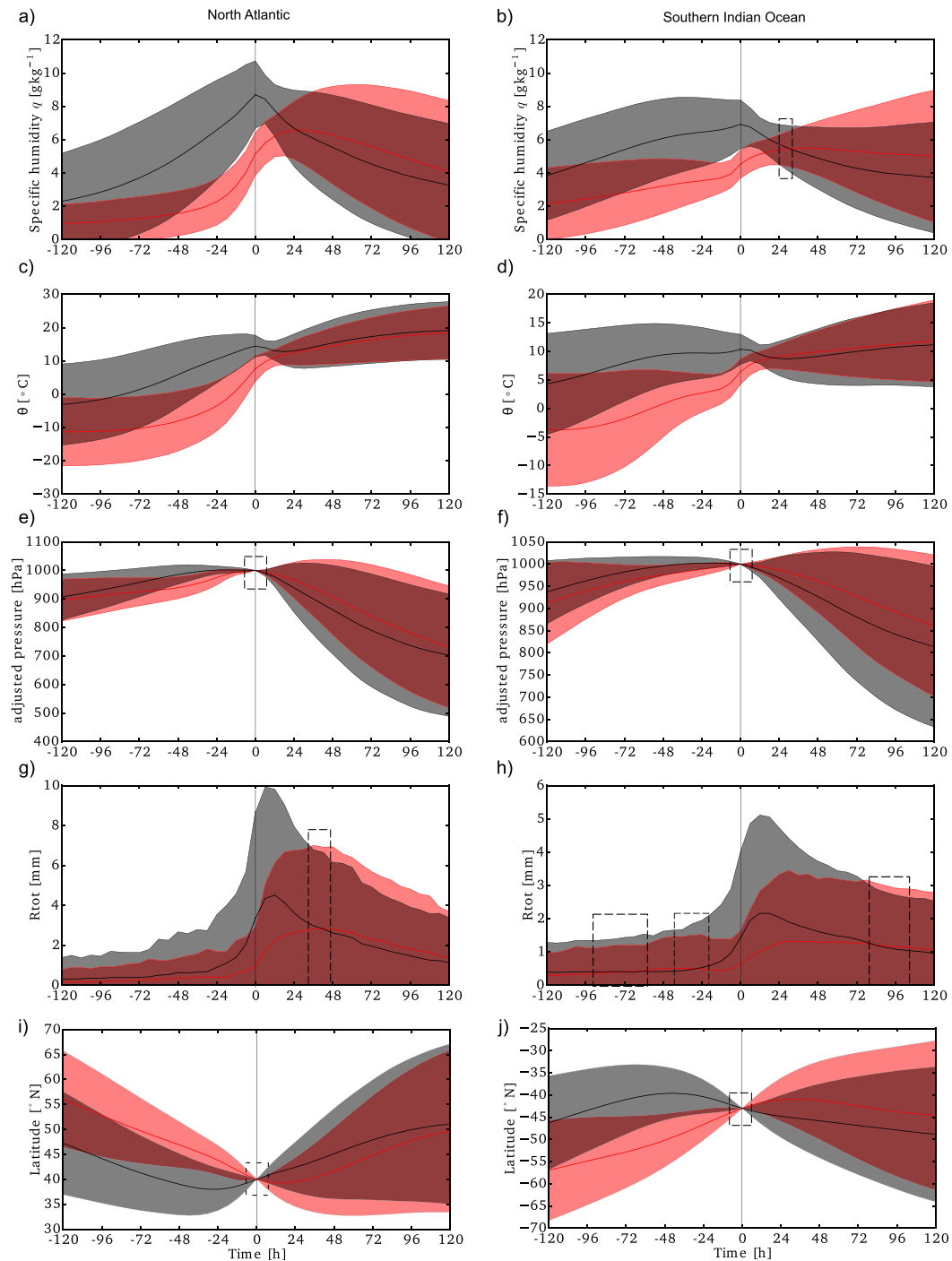
FIG. 9. Mean conditions (thick lines) and standard deviation (shaded area represents 2σ) along backward and forward trajectories started in (a),(c),(e),(g),(i) the North Atlantic (40°N, 60°W; DJF), and (b),(d),(f),(h),(j) the south Indian Ocean (43°S, 59°E; JJA). The conditions during SLOE at the starting point are shown in red and the conditions in the absence of SLOE are shown in gray. The starting points for the trajectory analysis are shown in Fig. 2. Periods during which the difference between the means of the two classes of data (for discrete 6-h time steps) is not significant ($p > 0.01$) based on a Welch's t test are highlighted with a dashed black box. For the North Atlantic (Southern Ocean), 8296 (6300) trajectories are associated with SLOE conditions and 4596 (6875) trajectories are associated with no-SLOE conditions.
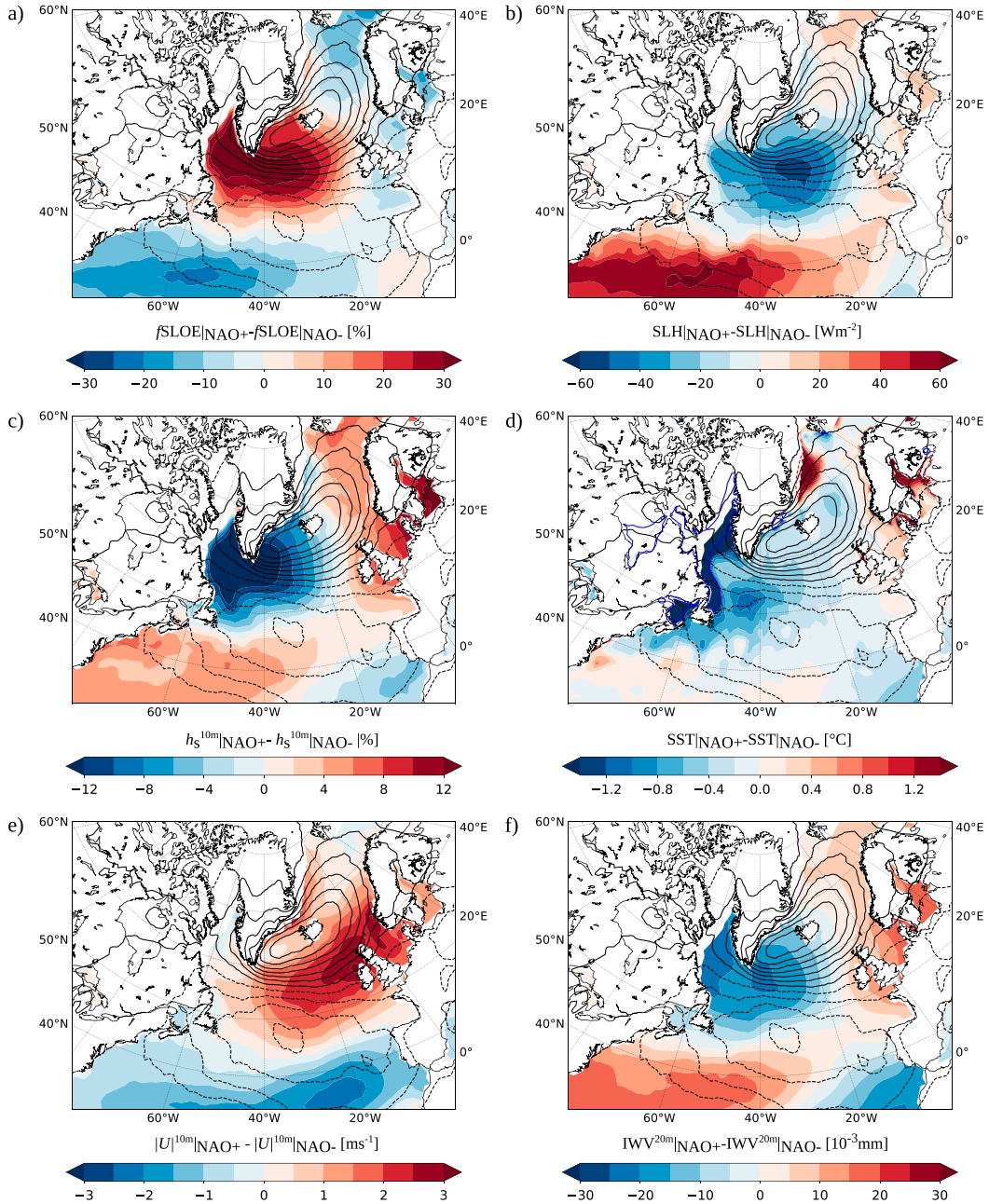
FIG. 10. Composite differences between NAO+ and NAO− based on monthly mean fields for DJF of (a) the SLOE frequency, (b) the SLH with negative values indicating an enhanced moisture flux from the ocean into the atmosphere, (c) h_s^{10m}, (d) SST, (e) $|U|^{10m}$, and (f) IWV^{20m}. The composite difference in cyclone frequency is shown in all panels in black contours (frequencies between −30% and 0% are shown by dashed contours and those between 0% and 30% by solid contours, in intervals of 5%). In (d) the colored contours additionally show the +10% (blue) and −10% (red) sea ice concentration anomalies. Regions with more than 50% sea ice are masked. (See Fig. C1 for JJA.)

black contours show changes in cyclone frequencies from NAO+ to NAO− years).

A markedly higher SLOE frequency (~20%–30%) can be observed in the Labrador and Irminger Seas and

the region south of Iceland (LISEI) during NAO+ years than NAO− (Fig. 10a). The strong positive SLOE anomaly during NAO+ years extends over nearly the whole North Atlantic from 45° to 65°N. Conversely,

along the Gulf Stream as well as across European coastal areas (in the Norwegian Sea, the North Sea, and the Bay of Biscay) the SLOE frequency is higher (~10%–20%) during NAO− years. The clearly stronger SLOE activity over the LISEI region during NAO+ is reflected in enhanced SLH (more negative values in Fig. 10b mean stronger heat loss of the ocean) during NAO+ resulting from the more frequent advection of dry polar air in the wake of the more frequent cyclones east of southern Greenland (lower IWV^{20m}; Fig. 10f) and larger humidity depletion values of the atmosphere (h_s^{10m}; Fig. 10c). More frequent tip jets (Våge et al. 2009) may further contribute to the strengthening of the SLHs to the southeast of Cape Farewell (southern tip of Greenland) during the NAO+ phase (Fig. 10e). Similarly, stronger barrier winds (Harden et al. 2011) may be responsible for the enhanced SLHs along the eastern Greenland coast.

In the regions of more frequent SLOE occurrence during NAO+, a negative anomaly in SST is generally observed (Fig. 10d) with up to 10% larger mean sea ice concentrations in the Labrador Sea. Potentially, evaporative cooling caused by stronger ocean evaporation and surface sensible heat fluxes plays an important role in the observed cooler ocean surface temperatures. A dynamically induced negative relation is thus found between ocean evaporation (enhanced) and SST (reduced) in the LISEI region during NAO+ (cf. Figs. 10b and 10d). For the same region, Gulev et al. (2013) showed that lower SST does not necessarily imply weaker ocean evaporation, as might be expected from a purely thermodynamical point of view when assuming that h_s^{10m} variations are small. These authors also found a negative relation between ocean evaporation and SST in the LISEI region to extend from the interannual to the decadal time scale.

b. SLOE variability associated with the SAM

The primary mode of variability in atmospheric circulation in the Southern Hemisphere is the SAM (Thompson and Wallace 2000). The southward shift of the storm track during positive phase SAM (SAM+) is reflected in an enhanced storminess in the seasonal sea ice region along the Antarctic coast (60°–80°S) and reduced cyclone frequencies at lower latitudes (Fig. 11a, black contours). The climatological cyclone frequency pattern off the Antarctic coast with the three peaks at 30°E, 100°E, and 160°W is reinforced during SAM+ (cf. black contours in Fig. 11 with Fig. 2a). Similar patterns in SAM–cyclone associations have been revealed by Pezza et al. (2012).

To the north of the maxima in the SAM+ cyclone frequency anomaly, two large-scale regions with a positive SLOE frequency anomaly with similar amplitude are found along the sea ice edge (Fig. 11a). Both SLOE frequency anomalies show collocated negative anomalies in IWV^{20m} associated with the reinforced advection of polar air in the cold sector of cyclones (Fig. 11f). Furthermore, the SLH from the ocean to the atmosphere is enhanced in these positive SLOE anomaly regions (Fig. 11b). Interestingly, this increase is to a large extent driven by stronger 10-m winds (Fig. 11e), whereas changes in h_s^{10m} are small (Fig. 11c) with clearly reduced values only near the sea ice edge in the south Indian Ocean (Davis Sea) and the Amundsen and Bellingshausen Seas. As in the LISEI region of the North Atlantic, the two hot spots of SAM-induced SLOE changes and enhanced ocean evaporation are collocated with slightly negative SST anomalies (Fig. 11d) and positive anomalies in sea ice concentration (blue contour in Fig. 11d).

The anomalies in SST and $|U|^{10m}$ shown in Figs. 11d and 11e are in line with the regression of air–sea variables onto the SAM at the interannual time scale (1985–2004) based on the satellite data of Lovenduski and Gruber (2005). Except for a weak asymmetry, the anomalies in the cyclone frequency and $|U|^{10m}$ with the SAM show a clear annular pattern. In contrast, the anomalies of the air–sea variables (the frequency of SLOE, SLH, h_s^{10m}, and IWV^{20m}; Figs. 11a–c,f) reveal a zonally nonuniform response. Similarly to the patterns found here, a zonally asymmetric response of the ocean mixed layer depth to SAM has been linked to changes in meridional winds, causing anomalies in the surface heat fluxes (Sallée et al. 2010). This indicates that slight changes in the location of the storm track and its associated frequency of cyclones can have important implications for the frequency of cold-air advection, evaporation in the cold sector of cyclones, and meridional moisture transport.

5. Discussion and conclusions

In this paper we have presented an object-based, global climatology (1979–2014) of events of strong atmospheric moisture uptake resulting from strong large-scale ocean evaporation (SLOE) and characterized by the typical atmospheric conditions in which these events take place. For the identification of SLOE we have employed a fixed-threshold criterion to the moisture uptake efficiency ($f_{evap} \geq 1.5\,h^{-1}$), which relates the ocean evaporation flux to the moisture content in a layer extending 20 m above the ocean surface. Our approach is not sensitive to the latitudinal gradient of SLH such that a globally constant threshold for SLOE identification can be used. Furthermore, the focus is laid on events
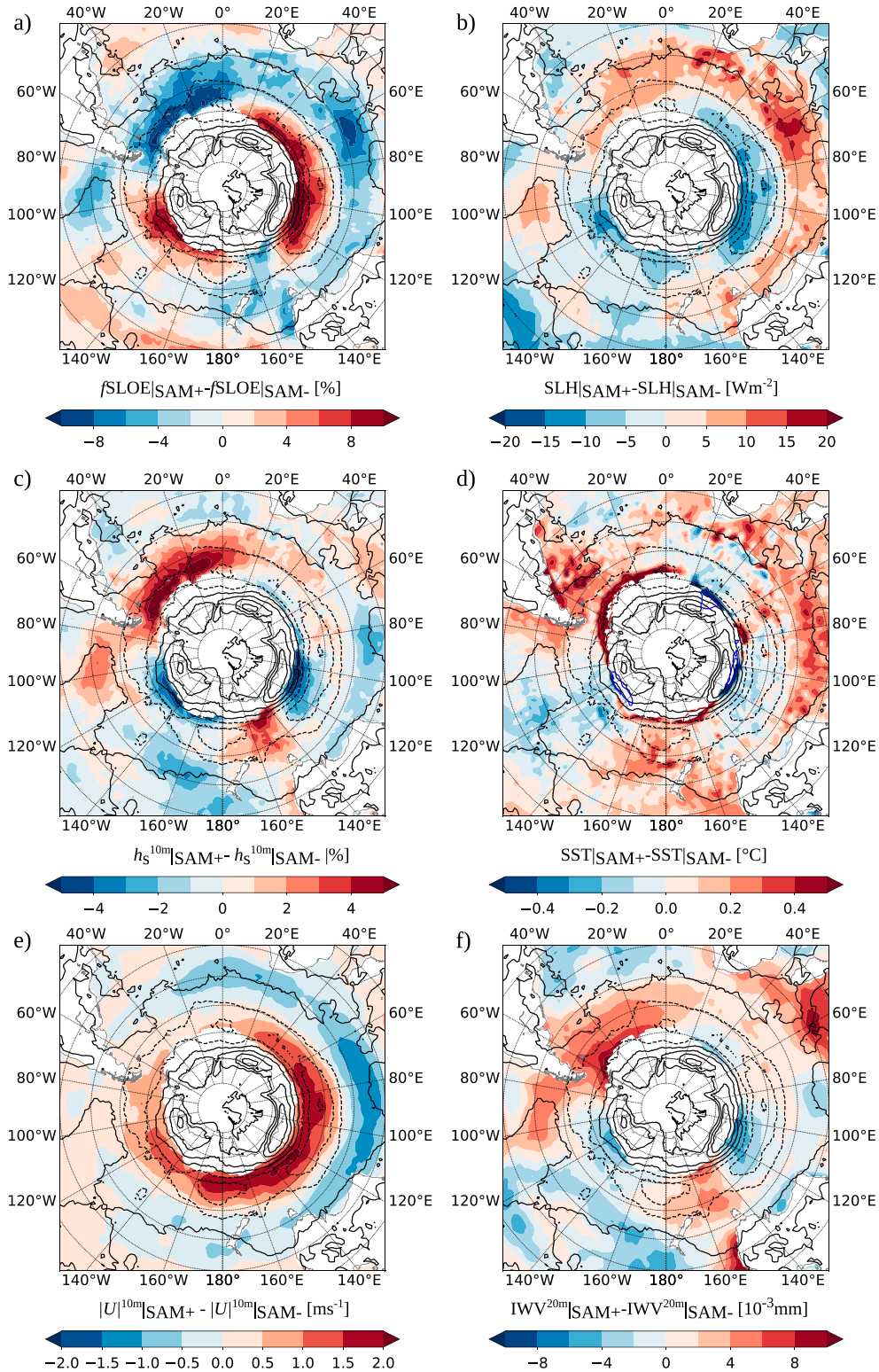
FIG. 11. As in Fig. 10, but for differences between SAM+ and SAM− based on monthly mean fields for JJA with the black contours, showing frequencies between −15% and 0% in dashed contours and between 0% and 15% in solid contours, in intervals of 5%. (See Fig. C2 for DJF.)

that together explain a large part of the total evaporation flux and not necessarily extremes of SLH. So-detected SLOE events predominantly occur during the cold season in association with cold-air advection on the rearward side of extratropical cyclones and with outbreaks of polar and/or continental air masses over open ocean. Hence, they are transient phenomena with a duration characteristic of the alternation time scale of warm and cold advection associated with baroclinic waves. Such events of short-lived intense evaporation explain nearly a quarter of the global annual mean ocean evaporation, even though they occur only 6% of the time in the global average. There are strong regional contrasts and clear hotspot areas of very frequent SLOE occurrence.

We have thus identified the following three distinct SLOE regimes: warm-ocean SLOE over the warm waters of the WBCs in both hemispheres, polar-air SLOE at high latitudes associated with polar CAOs, and wind-driven SLOE in regions with very high wind speeds induced by the interaction of extratropical cyclones with steep orography (e.g., in the Irminger Sea) or caused by the downward mixing of momentum in an unstably stratified boundary layer (e.g., the south Indian Ocean). The absolute amount of moisture uptake by the atmosphere in a single SLOE event is controlled by the vertical humidity gradient, which, following the approximately exponential Clausius–Clapeyron relation, is typically considerably larger for warm-ocean SLOE than for polar-air SLOE. The frequency of SLOE and the moisture uptake relative to the air parcel humidity, in contrast, is controlled by the humidity depletion state, which for both types of SLOE is about 20% below that observed under no-SLOE conditions. Wind-driven SLOE is controlled by the wind speed and features a less pronounced humidity depletion.

SLOE is far less frequent in the subtropics and inexistent in the tropics, where evaporation occurs in much more humid near-surface air masses than in the extratropics and at high latitudes, such that the moisture uptake efficiency is low. Subtropical SLOE is partly wind driven, but in the south Indian Ocean cold-air advection associated with elongated cold fronts also contributes. Furthermore, it may be in part associated with upper-level forced dry air intrusions. The influence of extratropical weather systems, and in particular the occurrence of dry intrusions in subtropical and tropical evaporation patterns, should be studied in more detail in the future.

A trajectory-based analysis over the Gulf Stream and in the south Indian Ocean has shown that the air masses leading to SLOE originate farther poleward, are drier and colder, and sink more strongly during the 72 h prior

to SLOE compared to no-SLOE air masses. After the strong moistening phase, SLOE air masses are associated with slightly more precipitation 2–5 days after the event than are no-SLOE air masses. Given the importance of latent heat release for the maintenance of baroclinicity along storm tracks (Papritz and Spengler 2015), SLOE air masses may thus play an important role for making baroclinicity available, for example, via the release of latent heat in the warm conveyor belt of extratropical cyclones. In fact, a dominant source of moisture for precipitation in warm conveyor belts of North Atlantic cyclones was shown to be located in a warm-water SLOE hot spot: the Gulf Stream (Pfahl et al. 2014). Since the majority of SLOE events over the Gulf Stream and the Kuroshio are induced by the passage of extratropical cyclones, SLOE might be an important factor contributing toward the self-maintenance of localized storm tracks, such as those in the North Atlantic and the North Pacific. The mechanistic pathway of the moisture that has been taken up during SLOE from its source into individual storms, however, remains unclear, as yet. Insight into the fate of the moisture could be gained with the help of combined humidity and stable water isotope measurements, as well as trajectory analysis.

From analyzing the observed anomalies in SLH, SST, $|U|^{10m}$, surface humidity gradient, and 20-m integrated water vapor associated with the respective leading atmospheric circulation variability modes in the North Atlantic and the Southern Ocean, it becomes clear that changes in regional evaporation patterns induced by cold-air advection cannot be deduced from thermodynamic steady-state considerations alone. Even though it seems intuitive that higher SSTs in a global warming scenario should lead to globally enhanced evaporation (Yu 2007), the mechanisms that control the regional covariations of SST, local air temperature, the surface humidity gradient, surface wind speed, and evaporation are not straightforward. The mean climate state and correlations between different climate variables might not reflect the conditions and covariations that characterize transient events of strong moisture input into the atmosphere through SLOE. This is particularly true for the hot spots of atmospheric moisture uptake lying along the storm tracks, where conditions change rapidly from cold- to warm-air advection and the air–sea moisture fluxes are alternating between strong moisture input and moisture depletion of the atmosphere. By focusing on individual events of strong ocean evaporation and their dynamical environment, the SLOE-based framework, presented here, offers an explanation for the negative relation between ocean evaporation and SST that has been previously identified

Backward trajectories location | Forward trajectories location
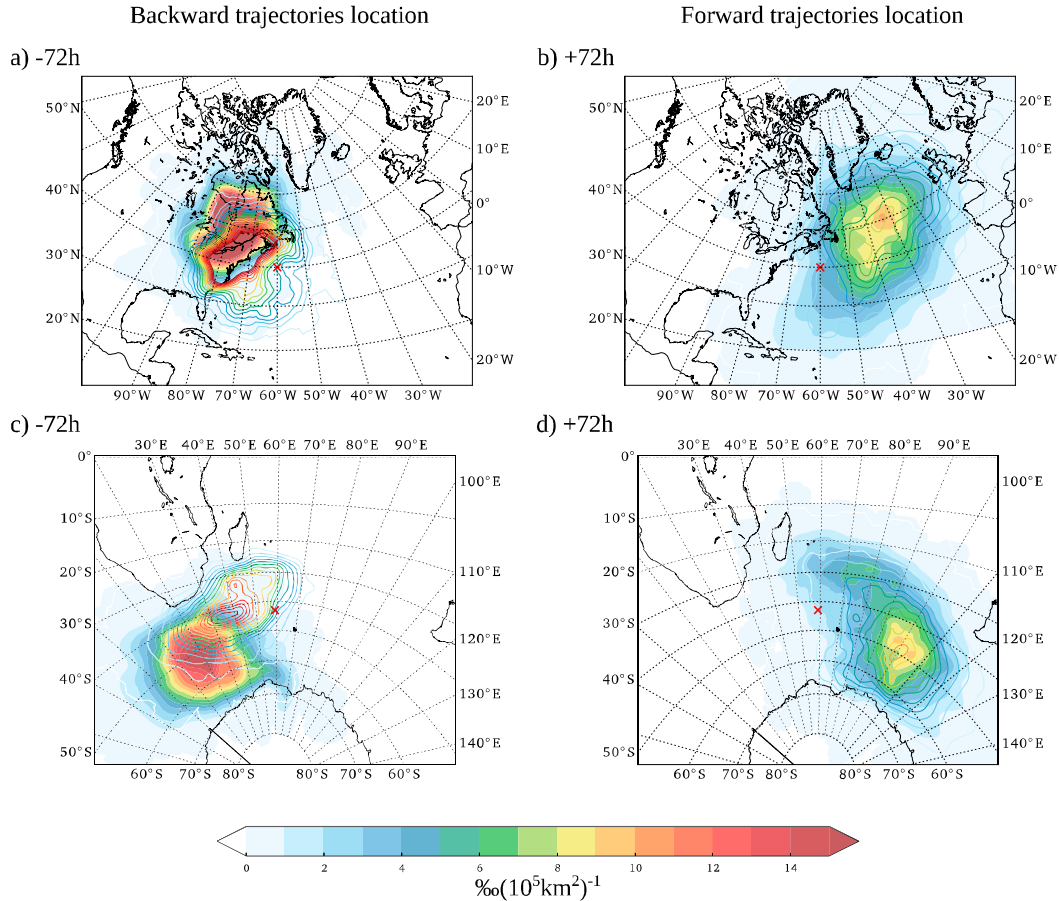

FIG. A1. (a),(c) Origin and (b),(d) fate of air masses leading to SLOE (color shading), and no-SLOE (colored contours), respectively, at $t_a = 0$ h for 72 h (a),(c) before and (b),(d) after arrival at 40°N, 60°W in the North Atlantic (red cross) in (a),(b) and 43°S, 59°E in the south Indian Ocean in (c),(d).

on the interannual–decadal time scale in a large region of the western North Atlantic between 45° and 65°N (Gulev et al. 2013). In addition, a similar negative relation between ocean evaporation and SST is found along the sea ice edge in the south Indian Ocean and the southern Pacific in connection with the SAM-induced southward shift of the storm track. The possible role of this negative relation for the extent of sea ice is the object of future research. Indeed, stronger winds and enhanced cooling of the ocean resulting from more frequent CAOs and SLOE in the ice growing season may be a contributor to the regionally increased sea ice concentration observed with trends toward a more positive SAM (Simmonds 2015; Kohyama and Hartmann 2016). A good mechanistic understanding of SAM-induced changes in air–sea interaction is key for reducing the large inter–climate model spread in the Southern Ocean SST response to a poleward intensification of the westerlies (Kostov et al. 2017).

Changes in SLOE frequencies might be registered in western Antarctic ice cores in regions with moisture sources from the meridionally oriented positive SLOE anomaly in the Pacific during SAM+ years. In eastern Antarctica an imprint of changing moisture source conditions from SAM might be different for low-elevation sites than for high-elevation sites. Low-elevation sites with moisture sources closer to Antarctica (Sodemann and Stohl 2009) probably reflect the positive SLOE anomalies observed for SAM+ years (Fig. 11a). In contrast, high-elevation sites with moisture sources from the midlatitudes (Sodemann and Stohl 2009) may instead reflect the positive SLOE anomalies for SAM− years (Fig. 11a). This aspect could be investigated in more detail in the future, using precipitation and surface snow isotope data from different sites across Antarctica.

Finally, from a centennial-time-scale perspective, changes in SLOE frequencies are expected if WBCs

change in intensity or storm tracks shift in latitudes as has been observed in past decades in response to global warming (Yang et al. 2016). This is a particularly relevant aspect for paleoclimatic applications such as changes in atmospheric moisture uptake and source patterns for Greenland and Antarctic precipitation in past climate reconstructions, for studying glacial–interglacial changes, as well as for freshwater forcing scenarios.

APPENDIX A

Origin and Fate of Air Masses Leading to SLOE Compared to No-SLOE Air Masses
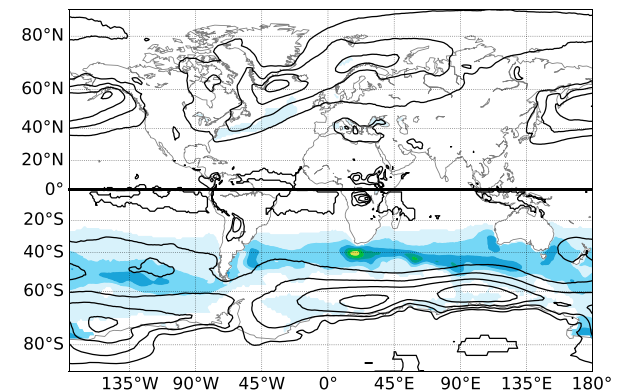
Figures A1a and A1b show gridded trajectory locations for air masses leading to SLOE (colored shading) compared to no SLOE (colored contours) for the point 40°N, 60°W in the North Atlantic, and similarly in Figs. A1c and A1d for the point 43°S, 59°E in the south Indian Ocean.

Overall, the airmass origin shows some clear differences between SLOE and no-SLOE air parcels, whereas the fate of SLOE versus no-SLOE trajectories seems to be similar. SLOE air masses originate from farther poleward than no-SLOE air masses (Figs. A1a,c). In the North Atlantic SLOE trajectories originate consistently over land, whereas an important fraction of no-SLOE air masses has a marine origin. In contrast, in the Southern Ocean this land–sea contrast does not exist and SLOE and no-SLOE air masses are distinct only by their latitude of origin.
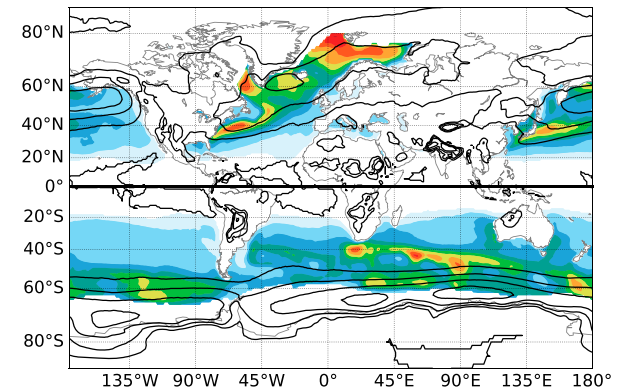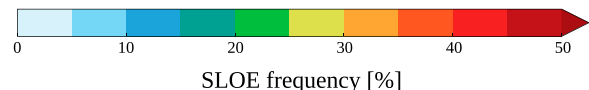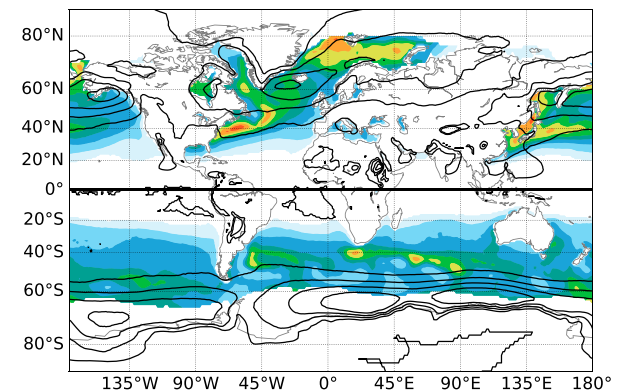

FIG. B1. SLOE occurrence frequencies (shading) during (a) spring (MAM in NH and SON in SH), (b) summer (JJA in NH and DJF in SH), and (c) autumn SON in NH and MAM in SH). The occurrence frequency of cyclones is shown from 10% to 40% in intervals of 10% (black contours). Land areas, regions with SLOE frequencies below 1%, or with seasonal sea ice are masked.
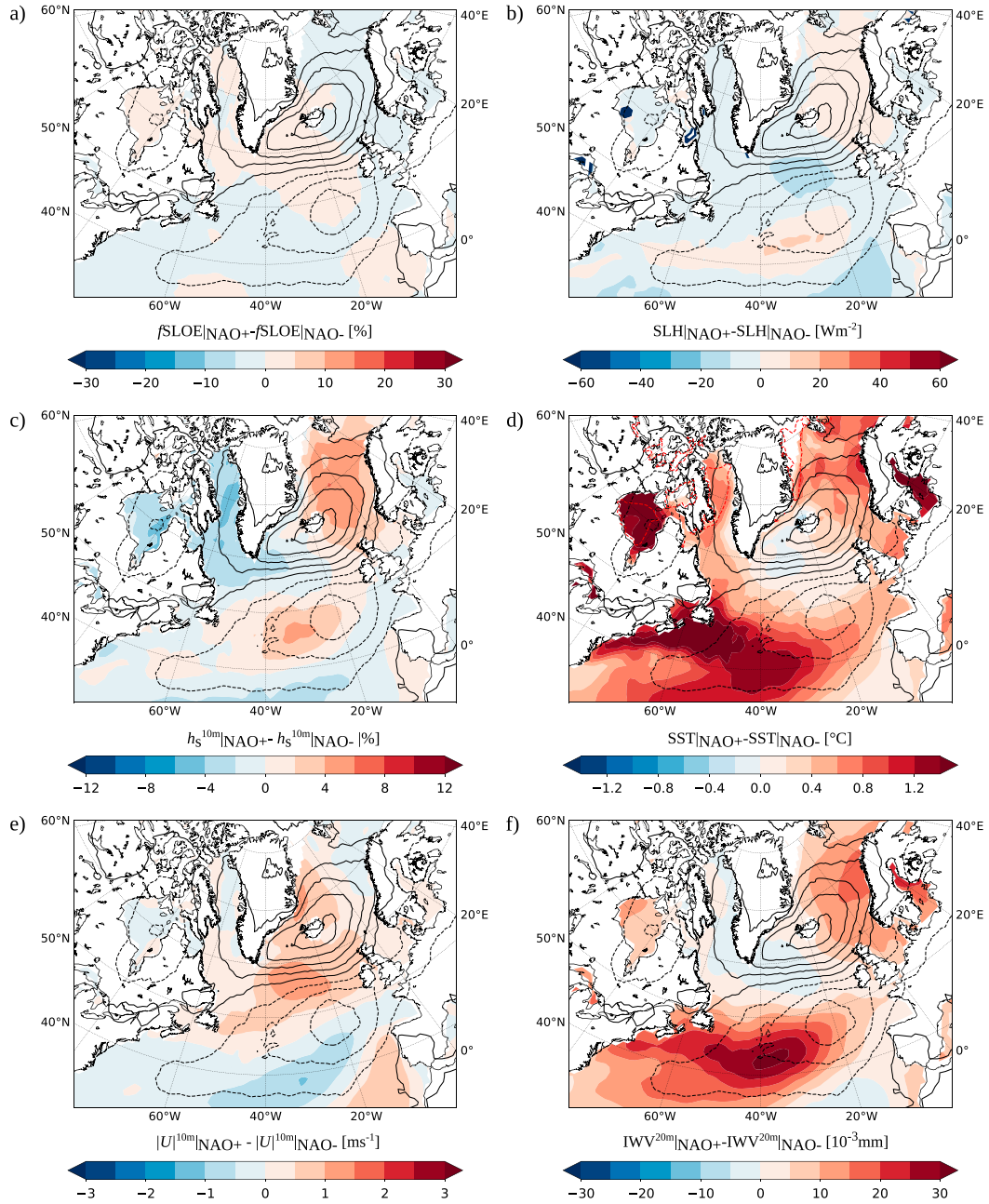
FIG. C1. As in Fig. 10, but for monthly mean fields for JJA.

APPENDIX B

Spring, Summer, and Autumn SLOE Occurrence Frequencies

Figure B1 shows the occurrence frequencies of SLOE for spring (MAM in NH and SON in SH), summer (JJA in NH and DJF in SH), and autumn (SON in NH and MAM in SH).

APPENDIX C

Summer Anomalies in Air–Sea Variables for the NAO- and SAM-Induced Anomalies

Figure C1 shows the composite differences in air–sea variables between NAO+ and NAO− conditions for JJA. Figure C2 shows the composite differences in air–sea variables between SAM+ and SAM− conditions for DJF.
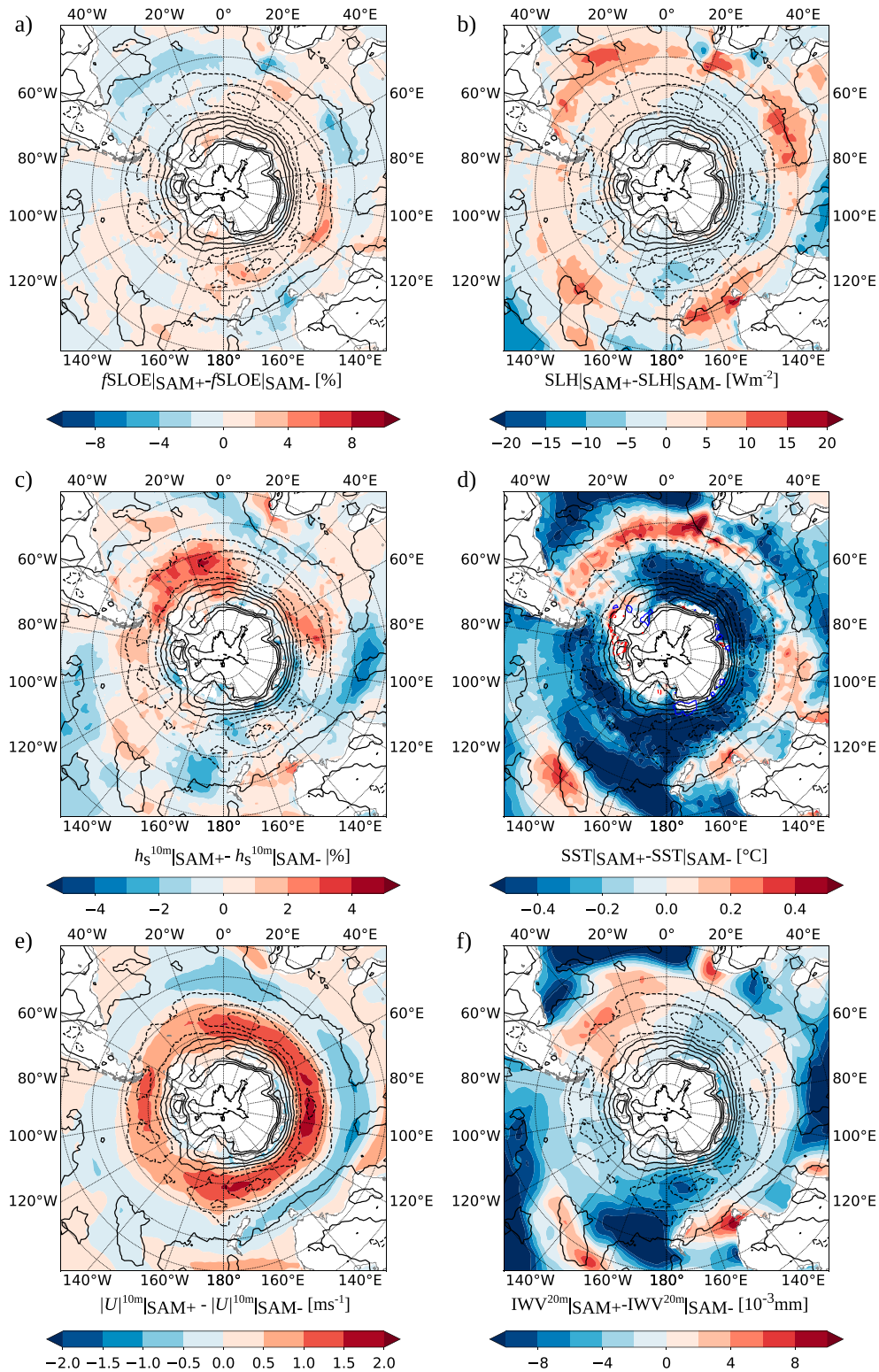
FIG. C2. As in Fig. 11, but for monthly mean fields for DJF.

REFERENCES

Aemisegger, F., 2013: Atmospheric stable water isotope measurements at the timescale of extratropical weather systems. Ph.D. dissertation 21165, ETH Zurich, Zurich, Switzerland, 242 pp., https://www.research-collection.ethz.ch/handle/20.500.11850/73321.

——, and J. Sjolte, 2018: A climatology of strong large-scale ocean evaporation events. Part II: Relevance for the deuterium excess signature of the evaporation flux. *J. Climate*, **31**, 7313–7336, https://doi.org/10.1175/JCLI-D-17-0592.1.

Appenzeller, C., T. F. Stocker, and M. Anklin, 1998: North Atlantic Oscillation dynamics recorded in Greenland ice cores. *Science*, **282**, 446–449, https://doi.org/10.1126/science.282.5388.446.

Baumgartner, A., and E. Reichel, 1975: *World Water Balance: Mean Annual Global, Continental and Maritime Precipitation, Evaporation and Runoff*. Elsevier, 182 pp.

Bentamy, A., and Coauthors, 2017: Review and assessment of latent and sensible heat flux accuracy over the global oceans. *Remote Sens. Environ.*, **201**, 196–218, https://doi.org/10.1016/j.rse.2017.08.016.

Blanton, J. O., J. A. Amft, D. K. Lee, and A. Riordan, 1989: Wind stress and heat fluxes observed during winter and spring 1986. *J. Geophys. Res.*, **94**, 10 686–10 698, https://doi.org/10.1029/JC094iC08p10686.

Bond, N. A., and R. G. Fleagle, 1988: Prefrontal and postfrontal boundary layer processes over the ocean. *Mon. Wea. Rev.*, **116**, 1257–1273, https://doi.org/10.1175/1520-0493(1988)116<1257:PAPBLP>2.0.CO;2.

Bracegirdle, T. J., and E. W. Kolstad, 2010: Climatology and variability of Southern Hemisphere marine cold-air outbreaks. *Tellus*, **62A**, 202–208, https://doi.org/10.1111/j.1600-0870.2009.00431.x.

Braham, R. R., Jr., 1952: The water and energy budgets of the thunderstorm and their relation to thunderstorm development. *J. Meteor.*, **9**, 227–242, https://doi.org/10.1175/1520-0469(1952)009<0227:TWAEBO>2.0.CO;2.

Brodeau, L., B. Barnier, S. K. Gulev, and C. Woods, 2017: Climatologically significant effects of some approximations in the bulk parameterizations of turbulent air–sea fluxes. *J. Phys. Oceanogr.*, **47**, 5–28, https://doi.org/10.1175/JPO-D-16-0169.1.

Browning, K. A., 1997: The dry intrusion perspective of extratropical cyclone development. *Meteor. Appl.*, **4**, 317–324, https://doi.org/10.1017/S1350482797000613.

Catto, J. L., and S. Pfahl, 2013: The importance of fronts for extreme precipitation. *J. Geophys. Res. Atmos.*, **118**, 10 791–10 801, https://doi.org/10.1002/jgrd.50852.

Cau, P., J. Methven, and B. Hoskins, 2007: Origins of dry air in the tropics and subtropics. *J. Climate*, **20**, 2745–2759, https://doi.org/10.1175/JCLI4176.1.

Craig, H., and L. Gordon, 1965: Deuterium and oxygen 18 variations in the ocean and the marine atmosphere. *Stable Isotopes in Oceanographic Studies and Paleotemperatures*, E. Tongiorgi, Ed., Laboratorio di Geologia Nucleare, 9–130.

Dee, D. P., and Coauthors, 2011: The ERA-Interim reanalysis: Configuration and performance of the data assimilation system. *Quart. J. Roy. Meteor. Soc.*, **137**, 553–597, https://doi.org/10.1002/qj.828.

——, M. Balmaseda, G. Balsamo, R. Engelen, A. J. Simmons, and J.-N. Thpaut, 2014: Toward a consistent reanalysis of the climate system. *Bull. Amer. Meteor. Soc.*, **95**, 1235–1248, https://doi.org/10.1175/BAMS-D-13-00043.1.

Doyle, J. D., and M. A. Shapiro, 1999: Flow response to large-scale topography: The Greenland tip jet. *Tellus*, **51A**, 728–748, https://doi.org/10.3402/tellusa.v51i5.14471.

ECMWF, 2007: Integrated Forecasting System's documentation, Part IV: Physical processes. IFS Documentation CY31R1, ECMWF, 155 pp.

Fasullo, J. T., and K. E. Trenberth, 2008: The annual cycle of the energy budget. Part II: Meridional structures and poleward transports. *J. Climate*, **21**, 2313–2325, https://doi.org/10.1175/2007JCLI1936.1.

Gat, J. R., B. Klein, Y. Kushnir, W. Roether, H. Wernli, R. Yam, and A. Shemesh, 2003: Isotope composition of air moisture over the Mediterranean Sea: An index of the air–sea interaction pattern. *Tellus*, **55B**, 953–965, https://doi.org/10.1034/j.1600-0889.2003.00081.x.

Gimeno, L., and Coauthors, 2012: Oceanic and terrestrial sources of continental precipitation. *Rev. Geophys.*, **50**, RG4003, https://doi.org/10.1029/2012RG000389.

Giordani, H., and G. Caniaux, 2001: Sensitivity of cyclogenesis to sea surface temperature in the northwestern Atlantic. *Mon. Wea. Rev.*, **129**, 1273–1295, https://doi.org/10.1175/1520-0493(2001)129<1273:SOCTSS>2.0.CO;2.

Grams, C. M., H. Binder, S. Pfahl, N. Piaget, and H. Wernli, 2014: Atmospheric processes triggering the central European floods in June 2013. *Nat. Hazards Earth Syst. Sci.*, **14**, 1691–1702, https://doi.org/10.5194/nhess-14-1691-2014.

Grist, J. P., S. A. Josey, Z. L. Jacobs, R. Marsh, B. Sinha, and E. Van Sebille, 2016: Extreme air–sea interaction over the North Atlantic subpolar gyre during the winter of 2013–2014 and its sub-surface legacy. *Climate Dyn.*, **46**, 4027–4045, https://doi.org/10.1007/s00382-015-2819-3.

Grossman, R. L., and A. K. Betts, 1990: Air–sea interaction during an extreme cold air outbreak from the eastern coast of the United States. *Mon. Wea. Rev.*, **118**, 324–342, https://doi.org/10.1175/1520-0493(1990)118<0324:AIDAEC>2.0.CO;2.

Gulev, S. K., and K. P. Belyaev, 2012: Probability distribution characteristics for surface air–sea turbulent heat fluxes over the global ocean. *J. Climate*, **25**, 184–206, https://doi.org/10.1175/2011JCLI4211.1.

——, M. Latif, N. Keenlyside, W. Park, and K. P. Koltermann, 2013: North Atlantic Ocean control on surface heat flux on multidecadal timescales. *Nature*, **499**, 464–467, https://doi.org/10.1038/nature12268.

Harden, B. E., I. A. Renfrew, and G. N. Petersen, 2011: A climatology of wintertime barrier winds off southeast Greenland. *J. Climate*, **24**, 4701–4717, https://doi.org/10.1175/2011JCLI4113.1.

Hausmann, U., A. Czaja, and J. Marshall, 2017: Mechanisms controlling the SST air–sea heat flux feedback and its dependence on spatial scale. *Climate Dyn.*, **48**, 1297–1307, https://doi.org/10.1007/s00382-016-3142-3.

Horita, J., K. Rozanski, and S. Cohen, 2008: Isotope effects in the evaporation of water: A status report of the Craig–Gordon model. *Isotopes Environ. Health Stud.*, **44**, 23–49, https://doi.org/10.1080/10256010801887174.

Hurrell, J. W., 1995: Decadal trends in the North Atlantic Oscillation: Regional temperatures and precipitation. *Science*, **269**, 676–679, https://doi.org/10.1126/science.269.5224.676.

Johnsen, S. J., W. Dansgaard, and J. W. C. White, 1989: The origin of Arctic precipitation under present and glacial conditions. *Tellus*, **41B**, 452–468, https://doi.org/10.1111/j.1600-0889.1989.tb00321.x.

Joussaume, S., R. Sadourny, and C. Vignal, 1986: Origin of precipitating water in a numerical simulation of the July climate. *Ocean–Air Interact.*, **1**, 43–56.

Kiehl, J. T., and K. E. Trenberth, 1997: Earth's annual global mean energy budget. *Bull. Amer. Meteor. Soc.*, **78**, 197–208, https://doi.org/10.1175/1520-0477(1997)078<0197:EAGMEB>2.0.CO;2.

Kohyama, T., and D. L. Hartmann, 2016: Antarctic sea ice response to weather and climate modes of variability. *J. Climate*, **29**, 721–741, https://doi.org/10.1175/JCLI-D-15-0301.1.

Kolstad, E. W., T. J. Bracegirdle, and I. A. Seierstad, 2009: Marine cold-air outbreaks in the North Atlantic: Temporal distribution and associations with large-scale atmospheric circulation. *Climate Dyn.*, **33**, 187–197, https://doi.org/10.1007/s00382-008-0431-5.

Koster, R., J. Jouzel, R. Suozzo, G. Russell, W. Broecker, D. Rind, and P. Eagleson, 1986: Global sources of local precipitation as determined by the NASA/GISS GCM. *Geophys. Res. Lett.*, **13**, 121–124, https://doi.org/10.1029/GL013i002p00121.

Kostov, Y., J. Marshall, U. Hausmann, K. C. Armour, D. Ferreira, and M. M. Holland, 2017: Fast and slow responses of Southern Ocean sea surface temperature to SAM in coupled climate models. *Climate Dyn.*, **48**, 1595–1609, https://doi.org/10.1007/s00382-016-3162-z.

Kurita, N., 2011: Origin of Arctic water vapor during the ice-growth season. *Geophys. Res. Lett.*, **38**, L02709, https://doi.org/10.1029/2010GL046064.

Kuwano-Yoshida, A., and S. Minobe, 2017: Storm-track response to SST fronts in the northwestern Pacific region in an AGCM. *J. Climate*, **30**, 1081–1102, https://doi.org/10.1175/JCLI-D-16-0331.1.

Lindsay, R., M. Wensnahan, A. Schweiger, and J. Zhang, 2014: Evaluation of seven different atmospheric reanalysis products in the Arctic. *J. Climate*, **27**, 2588–2606, https://doi.org/10.1175/JCLI-D-13-00014.1.

Lovenduski, N. S., and N. Gruber, 2005: Impact of the Southern Annular Mode on Southern Ocean circulation and biology. *Geophys. Res. Lett.*, **32**, L11603, https://doi.org/10.1029/2005GL022727.

Marshall, G. J., 2003: Trends in the southern annular mode from observations and reanalyses. *J. Climate*, **16**, 4134–4143, https://doi.org/10.1175/1520-0442(2003)016<4134:TITSAM>2.0.CO;2.

Massacand, A. C., H. Wernli, and H. C. Davies, 1998: Heavy precipitation on the alpine southside: An upper-level precursor. *Geophys. Res. Lett.*, **25**, 1435–1438, https://doi.org/10.1029/98GL50869.

Mayer, M., and L. Haimberger, 2012: Poleward atmospheric energy transports and their variability as evaluated from ECMWF reanalysis data. *J. Climate*, **25**, 734–752, https://doi.org/10.1175/JCLI-D-11-00202.1.

Moore, G. W. K., and I. A. Renfrew, 2002: An assessment of the surface turbulent heat fluxes from the NCEP–NCAR reanalysis over western boundary currents. *J. Climate*, **15**, 2020–2037, https://doi.org/10.1175/1520-0442(2002)015<2020:AAOTST>2.0.CO;2.

——, and R. S. Pickart, 2012: Northern Bering Sea tip jets. *Geophys. Res. Lett.*, **39**, L08807, https://doi.org/10.1029/2012GL051537.

Noone, D., and I. Simmonds, 2002: Annular variations in moisture transport mechanisms and the abundance of δ^{18}O in Antarctic snow. *J. Geophys. Res.*, **107**, 4742, https://doi.org/10.1029/2002JD002262.

Papritz, L., 2017: Synoptic environments and characteristics of cold air outbreaks in the Irminger Sea. *Int. J. Climatol.*, **37**, 193–207, https://doi.org/10.1002/joc.4991.

——, and T. Spengler, 2015: Analysis of the slope of isentropic surfaces and its tendencies over the North Atlantic. *Quart. J. Roy. Meteor. Soc.*, **141**, 3226–3238, https://doi.org/10.1002/qj.2605.

——, and ——, 2017: A Lagrangian climatology of wintertime cold air outbreaks in the Irminger and Nordic seas and their role in shaping air–sea heat fluxes. *J. Climate*, **31**, 2717–2737, https://doi.org/10.1175/JCLI-D-16-0605.1.

——, S. Pfahl, I. Rudeva, I. Simmonds, H. Sodemann, and H. Wernli, 2014: The role of extratropical cyclones and fronts for Southern Ocean freshwater fluxes. *J. Climate*, **27**, 6205–6224, https://doi.org/10.1175/JCLI-D-13-00409.1.

——, ——, H. Sodemann, and H. Wernli, 2015: A climatology of cold air outbreaks and their impact on air–sea heat fluxes in the high-latitude South Pacific. *J. Climate*, **28**, 342–364, https://doi.org/10.1175/JCLI-D-14-00482.1.

Parfitt, R., A. Czaja, and Y.-O. Kwon, 2017: The impact of SST resolution change in the ERA-Interim reanalysis on wintertime Gulf Stream frontal air-sea interaction. *Geophys. Res. Lett.*, **44**, 3246–3254, https://doi.org/10.1002/2017GL073028.

Persson, P. O. G., J. E. Hare, C. W. Fairall, and W. D. Otto, 2005: Air–sea interaction processes in warm and cold sectors of extratropical cyclonic storms observed during FASTEX. *Quart. J. Roy. Meteor. Soc.*, **131**, 877–912, https://doi.org/10.1256/qj.03.181.

Pezza, A. B., H. A. Rashid, and I. Simmonds, 2012: Climate links and recent extremes in Antarctic sea ice high-latitude cyclones, southern annular mode and ENSO. *Climate Dyn.*, **38**, 57–73, https://doi.org/10.1007/s00382-011-1044-y.

Pezzi, L. P., R. B. Souza, P. C. Farias, O. Acevedo, and A. J. Miller, 2016: Air-sea interaction at the Southern Brazilian Continental Shelf: In situ observations. *J. Geophys. Res. Oceans*, **121**, 6671–6695, https://doi.org/10.1002/2016JC011774.

Pfahl, S., and N. Niedermann, 2011: Daily covariations in near-surface relative humidity and temperature over the ocean. *J. Geophys. Res.*, **116**, D19104, https://doi.org/10.1029/2011JD015792.

——, and H. Wernli, 2012: Quantifying the relevance of cyclones for precipitation extremes. *J. Climate*, **25**, 6770–6780, https://doi.org/10.1175/JCLI-D-11-00705.1.

——, E. Madonna, M. Boettcher, H. Joos, and H. Wernli, 2014: Warm conveyor belts in the ERA-Interim dataset (1979–2010). Part II: Moisture origin and relevance for precipitation. *J. Climate*, **27**, 27–40, https://doi.org/10.1175/JCLI-D-13-00223.1.

Rasmussen, E. A., and J. Turner, 2003: *Polar Lows: Mesoscale Weather Systems in the Polar Regions.* Cambridge University Press, 628 pp.

Raveh-Rubin, S., 2017: Dry intrusions: Lagrangian climatology and dynamical impact on the planetary boundary layer. *J. Climate*, **30**, 6661–6682, https://doi.org/10.1175/JCLI-D-16-0782.1.

Reed, R. J., G. A. Grell, and Y.-H. Kuo, 1993: The ERICA IOP 5 storm. Part I: Analysis and simulation. *Mon. Wea. Rev.*, **121**, 1577–1594, https://doi.org/10.1175/1520-0493(1993)121<1577:TEISPI>2.0.CO;2.

Renfrew, I. A., G. W. K. Moore, P. S. Guest, and K. Bumke, 2002: A comparison of surface layer and surface turbulent flux observations over the Labrador Sea with ECMWF analyses and NCEP reanalyses. *J. Phys. Oceanogr.*, **32**, 383–400, https://doi.org/10.1175/1520-0485(2002)032<0383:ACOSLA>2.0.CO;2.

——, G. N. Petersen, D. J. Sproson, G. W. K. Moore, H. Adiwidjaja, S. Zhang, and R. North, 2009: A comparison of aircraft-based surface-layer observations over Denmark Strait and the Irminger Sea with meteorological analyses and QuikSCAT winds. *Quart. J. Roy. Meteor. Soc.*, **135**, 2046–2066, https://doi.org/10.1002/qj.444.

Rouault, M., C. J. C. Reason, J. R. E. Lutjeharms, and A. C. M. Beljaars, 2003: Underestimation of latent and sensible heat fluxes above the Agulhas Current in NCEP and ECMWF analyses. *J. Climate*, **16**, 776–782, https://doi.org/10.1175/1520-0442(2003)016<0776:UOLASH>2.0.CO;2.

Rudeva, I., and S. K. Gulev, 2011: Composite analysis of North Atlantic extratropical cyclones in NCEP–NCAR reanalysis data. *Mon. Wea. Rev.*, **139**, 1419–1446, https://doi.org/10.1175/2010MWR3294.1.

——, and I. Simmonds, 2015: Variability and trends of global atmospheric frontal activity and links with large-scale modes of variability. *J. Climate*, **28**, 3311–3330, https://doi.org/10.1175/JCLI-D-14-00458.1.

Sallée, J. B., K. G. Speer, and S. R. Rintoul, 2010: Zonally asymmetric response of the Southern Ocean mixed-layer depth to the southern annular mode. *Nat. Geosci.*, **3**, 273–279, https://doi.org/10.1038/ngeo812.

Sampe, T., and S.-P. Xie, 2007: Mapping high sea winds from space: A global climatology. *Bull. Amer. Meteor. Soc.*, **88**, 1965–1978, https://doi.org/10.1175/BAMS-88-12-1965.

Schemm, S., I. Rudeva, and I. Simmonds, 2015: Extratropical fronts in the lower troposphere–global perspectives obtained from two automated methods. *Quart. J. Roy. Meteor. Soc.*, **141**, 1686–1698, https://doi.org/10.1002/qj.2471.

Schmitt, R. W., 1995: The ocean component of the global water cycle. *Rev. Geophys.*, **33** (S2), 1395–1409, https://doi.org/10.1029/95RG00184.

Schneider, T., P. A. O'Gorman, and X. J. Levine, 2010: Water vapor and the dynamics of climate changes. *Rev. Geophys.*, **48**, RG3001, https://doi.org/10.1029/2009RG000302.

Shaw, T. A., and Coauthors, 2016: Storm track processes and the opposing influences of climate change. *Nat. Geosci.*, **9**, 656–665, https://doi.org/10.1038/ngeo2783.

Simmonds, I., 2015: Comparing and contrasting the behaviour of Arctic and Antarctic sea ice over the 35 year period 1979-2013. *Ann. Glaciol.*, **56** (69), 18–28, https://doi.org/10.3189/2015AoG69A909.

——, and M. Dix, 1989: The use of mean atmospheric parameters in the calculation of modeled mean surface heat fluxes over the world's oceans. *J. Phys. Oceanogr.*, **19**, 205–215, https://doi.org/10.1175/1520-0485(1989)019<0205:TUOMAP>2.0.CO;2.

——, K. Keay, and J. A. T. Bye, 2012: Identification and climatology of Southern Hemisphere mobile fronts in a modern reanalysis. *J. Climate*, **25**, 1945–1962, https://doi.org/10.1175/JCLI-D-11-00100.1.

Simmons, A. J., K. M. Willett, P. D. Jones, P. W. Thorne, and D. P. Dee, 2010: Low-frequency variations in surface atmospheric humidity, temperature, and precipitation: Inferences from reanalyses and monthly gridded observational data sets. *J. Geophys. Res.*, **115**, D01110, https://doi.org/10.1029/2009JD012442.

Sjolte, J., G. Hoffmann, S. J. Johnsen, B. M. Vinther, V. Masson-Delmotte, and C. Sturm, 2011: Modeling the water isotopes in Greenland precipitation 1959–2001 with the meso-scale model REMO-iso. *J. Geophys. Res.*, **116**, D18105, https://doi.org/10.1029/2010JD015287.

Sodemann, H., and A. Stohl, 2009: Asymmetries in the moisture origin of Antarctic precipitation. *Geophys. Res. Lett.*, **36**, L22803, https://doi.org/10.1029/2009GL040242.

——, C. Schwierz, and H. Wernli, 2008a: Interannual variability of Greenland winter precipitation sources: Lagrangian moisture diagnostic and North Atlantic Oscillation influence. *J. Geophys. Res.*, **113**, D03107, https://doi.org/10.1029/2007JD008503.

——, V. Masson-Delmotte, C. Schwierz, B. M. Vinther, and H. Wernli, 2008b: Interannual variability of Greenland winter precipitation sources: 2. Effects of North Atlantic Oscillation variability on stable isotopes in precipitation. *J. Geophys. Res.*, **113**, D12111, https://doi.org/10.1029/2007JD009416.

——, H. Wernli, and C. Schwierz, 2009: Sources of water vapour contributing to the Elbe flood in August 2002—A tagging study in a mesoscale model. *Quart. J. Roy. Meteor. Soc.*, **135**, 205–223, https://doi.org/10.1002/qj.374.

Sprenger, M., and H. Wernli, 2015: The LAGRANTO Lagrangian analysis tool – version 2.0. *Geosci. Model Dev.*, **8**, 2569–2586, https://doi.org/10.5194/gmd-8-2569-2015.

——, and Coauthors, 2017: Global climatologies of Eulerian and Lagrangian flow features based on ERA-Interim. *Bull. Amer. Meteor. Soc.*, **98**, 1739–1748, https://doi.org/10.1175/BAMS-D-15-00299.1.

Talley, L. D., 2008: Freshwater transport estimates and the global overturning circulation: Shallow, deep and throughflow components. *Prog. Oceanogr.*, **78**, 257–303, https://doi.org/10.1016/j.pocean.2008.05.001.

Thompson, D. W. J., and J. M. Wallace, 2000: Annular modes in the extratropical circulation. Part I: Month-to-month variability. *J. Climate*, **13**, 1000–1016, https://doi.org/10.1175/1520-0442(2000)013<1000:AMITEC>2.0.CO;2.

Trenberth, K. E., and J. M. Caron, 2001: Estimates of meridional atmosphere and ocean heat transports. *J. Climate*, **14**, 3433–3443, https://doi.org/10.1175/1520-0442(2001)014<3433:EOMAAO>2.0.CO;2.

——, ——, and D. P. Stepaniak, 2001: The atmospheric energy budget and implications for surface fluxes and ocean heat transports. *Climate Dyn.*, **17**, 259–276, https://doi.org/10.1007/PL00007927.

——, J. T. Fasullo, and J. Mackaro, 2011: Atmospheric moisture transports from ocean to land and global energy flows in reanalyses. *J. Climate*, **24**, 4907–4924, https://doi.org/10.1175/2011JCLI4171.1.

Uotila, P., T. Vihma, A. B. Pezza, I. Simmonds, K. Keay, and A. H. Lynch, 2011: Relationships between Antarctic cyclones and surface conditions as derived from high-resolution numerical weather prediction data. *J. Geophys. Res.*, **116**, D07109, https://doi.org/10.1029/2008JD010209.

Våge, K., T. Spengler, H. C. Davies, and R. S. Pickart, 2009: Multi-event analysis of the westerly Greenland tip jet based upon 45 winters in ERA-40. *Quart. J. Roy. Meteor. Soc.*, **135**, 1999–2011, https://doi.org/10.1002/qj.488.

Vannière, B., A. Czaja, H. Dacre, and T. Woollings, 2017: A "cold path" for the Gulf Stream–troposphere connection. *J. Climate*, **30**, 1363–1379, https://doi.org/10.1175/JCLI-D-15-0749.1.

Vinther, B. M., S. J. Johnsen, K. K. Andersen, H. B. Clausen, and A. W. Hansen, 2003: NAO signal recorded in the stable isotopes of Greenland ice cores. *Geophys. Res. Lett.*, **30**, 1387, https://doi.org/10.1029/2002GL016193.

Walker, G. T., and E. W. Bliss, 1928: World weather IV: Some applications to seasonal foreshadowing. *Mem. Roy. Meteor. Soc.*, **3**, 81–95.

Wernli, H., and H. C. Davies, 1997: A Lagrangian-based analysis of extratropical cyclones. I: The method and some applications. *Quart. J. Roy. Meteor. Soc.*, **123**, 467–489, https://doi.org/10.1002/qj.49712353811.

——, and C. Schwierz, 2006: Surface cyclones in the ERA-40 dataset (1958–2001). Part I: Novel identification method and global climatology. *J. Atmos. Sci.*, **63**, 2486–2507, https://doi.org/10.1175/JAS3766.1.

White, J. W. C., L. K. Barlow, D. Fisher, P. Grootes, J. Jouzel, S. J. Johnsen, M. Stuiver, and H. Clausen, 1997: The climate signal in

the stable isotopes of snow from Summit, Greenland: Results of comparisons with modern climate observations. *J. Geophys. Res.*, **102**, 26 425–26 439, https://doi.org/10.1029/97JC00162.

Winschall, A., S. Pfahl, H. Sodemann, and H. Wernli, 2012: Impact of North Atlantic evaporation hot spots on southern Alpine heavy precipitation events. *Quart. J. Roy. Meteor. Soc.*, **138**, 1245–1258, https://doi.org/10.1002/qj.987.

Yang, H., G. Lohmann, W. Wei, M. Dima, M. Ionita, and J. Liu, 2016: Intensification and poleward shift of subtropical western boundary currents in a warming climate. *J. Geophys. Res. Oceans*, **121**, 4928–4945, https://doi.org/10.1002/2015JC011513.

Yau, M. K., and M. Jean, 1989: Synoptic aspects and physical processes in the rapidly intensifying cyclone of 6–8 March 1986. *Atmos.–Ocean*, **27**, 59–86, https://doi.org/10.1080/07055900.1989.9649328.

Yu, L., 2007: Global variations in oceanic evaporation (1958–2005): The role of the changing wind speed. *J. Climate*, **20**, 5376–5390, https://doi.org/10.1175/2007JCLI1714.1.

Yuan, X., J. Patoux, and C. Li, 2009: Satellite-based midlatitude cyclone statistics over the Southern Ocean: 2. Tracks and surface fluxes. *J. Geophys. Res.*, **114**, D04106, https://doi.org/10.1029/2008JD010874.